FEASIBILITY STUDY OF RADIO FREQUENCY MICROELECTROMECHANICAL FILTERS FOR SPACE APPLICATIONS

THESIS

Karanvir Singh, First Lieutenant, USAF

AFIT-ENG-MS-21-J-016

DEPARTMENT OF THE AIR FORCE
AIR UNIVERSITY

AIR FORCE INSTITUTE OF TECHNOLOGY

Wright-Patterson Air Force Base, Ohio

AFIT-ENG-MS-21-J-016

FEASIBILITY STUDY OF RADIO FREQUENCY MICROELECTROMECHANICAL FILTERS FOR SPACE APPLICATIONS

THESIS

Presented to the Faculty

Department of Electrical and Computer Engineering

Graduate School of Engineering and Management

Air Force Institute of Technology

Air University

Air Education and Training Command

In Partial Fulfillment of the Requirements for the

Degree of Master of Science in Electrical Engineering

Karanvir Singh, First Lieutenant, B.S.E.E.

First Lieutenant, USAF

June 2021

AFIT-ENG-MS-21-J-016

FEASIBILITY STUDY OF RADIO FREQUENCY MICROELECTROMECHANICAL FILTERS FOR SPACE APPLICATIONS

Karanvir Singh, B.S.E.E.

First Lieutenant, USAF

Committee Membership:

Dr. Hengky Chandrahalim, PhD
Chair

Dr. Matthew Vincie, PhD
Member

Dr. Kevin Leedy, PhD
Member

AFIT-ENG-MS-21-J-016

Abstract

Piezoelectric contour mode resonator technology has the unique advantage of combining low motional resistance with the ability to define multiple frequencies on the same substrate. Contour mode resonators can be mechanically coupled together to form robust band-pass filters for the next generation of GPS satellites with extreme size reduction compared to electrically coupled filters. Piezoelectric zinc oxide (ZnO) contour mode resonators have the potential for monolithic integration with current ZnO transistor further reducing size, power consumption, and cost of filter modules. Barium strontium titanate (BST) contour mode resonators have incredible frequency tunability due to the fundamental nature of the thin film in the presence of a DC bias. BST resonators can be intrinsically switched on and off with the application of a DC bias. Through this research, the feasibility of the design and fabrication of piezoelectric radio frequency (RF) microelectromechanical system (MEMS) filters using ZnO, BST, and metals with high melting points is presented.

This work is dedicated to my family, friends and mentors who have supported me and guided me through my time at AFIT.

Acknowledgments

I would like to express my sincere appreciation towards my faculty advisor, Dr. Hengky Chandrahalim, for his guidance and support throughout the course of this thesis effort. There were certainly many challenging times throughout the research period, but your unwavering attitude and dedication to your craft helped me accomplish all my academic goals. To my committee members, Dr. Matthew Vincie and Dr. Kevin Leedy, thank you for your continued support and feedback for my thesis. Thank you Dr. Leedy for all your time and effort to help me with material depositions. To my family and friends, thank you for your endless emotional support. Thank you for listening to my daily complaints and offering me much needed words of encouragement.

Karanvir Singh

Table of Contents

Page

List of Figures

Page

List of Tables

Page

List of Acronyms

BST	Barium Strontium Titanate
BVD	Butterworth-Van Dyke
FEA	Finite Elemental Analysis
LEM	Length Extensional Mode
MEMS	Microelectromechanical Systems
PZT	Lead Zirconate Titanate
Q	Quality Factor
RF	Radio Frequency
RIE	Reactive Ion Etching
SAW	Surface Acoustic Wave
SEM	Scanning Electron Microscope
SOLT	Short, Open, Load, Through
WEM	Width Extensional Mode
XRD	X-Ray Diffraction
ZnO	Zinc Oxide

FEASIBILITY STUDY OF RADIO FREQUENCY MICROELECTROMECHANICAL FILTERS FOR SPACE APPLICATIONS

I. Introduction

1.1 Overview

Microelectromechanical Systems (MEMS) are extremely prevalent in today's modern electronic systems. MEMS technologies are utilized in numerous sectors such as the automotive industry, healthcare, energy harvesting, inkjet printing, and especially radio frequency (RF) communications systems. MEMS devices, as compared to past solutions, offer low cost, high performance, and a condensed footprint in key RF systems. Past communications systems have relied on quartz crystals for RF synthesis and filtering needs.[1] The work in this thesis will study vibrating piezoelectric and ferroelectric materials to be used in bulk acoustic wave resonators operating in the L-band. The resonators will be designed using compatible metal electrodes targeted for operation in harsh space environments.

1.2 Motivation

The goal for this thesis is to explore and identify potential electromechanical transducer materials and compatible metals for frequency tunable RF MEMS filters that can operate at L-band frequency spectrum and exhibit insertion losses that meet the next generation GPS satellite navigation payload requirements. The fundamental objective of this thesis is to study the feasibility of the design and fabrication of RF MEMS filters using zinc oxide (ZnO) and barium strontium titanate (BST) as the electromechanical transducer materials.

The forthcoming GPS satellites are targeted on becoming more compact and much less power hungry with several enhancements to the way the satellites generate navigation signals. These GPS satellites need to employ digital beam forming elements and direct digital synthesizers that have compact dimensions, miniscule weight, low power demands, and robustness to shocks, vibrations, and temperature variations. They demand high-performance tunable filters and filter banks to generate signals with dynamic waveforms and bandwidths within the L-band frequency spectrum.

Piezoelectric RF MEMS filters exhibit potential to be utilized in space applications.[2] These filters have been mainly designed with lead zirconate titanate (PZT) as the transduction material. PZT has been the choice piezoelectric for many decades due to its highly desired characteristics. PZT offers a high dielectric constant and has a unique ability to improve the sensitivity of the filters.[3] The tunable RF MEMS filters created with PZT demonstrate a great applicability for digital beam forming elements. However, the trend recently has been to avoid lead based piezoelectric material due to environmental concerns.[4]

A ZnO or BST contour-mode RF MEMS resonator is believed to be an excellent constituent resonator to realize such filter banks because it has a high-quality factor and a frequency of operation that can be defined lithographically. Additionally, ZnO RF MEMS resonators can be monolithically integrated with ZnO transistor to allow production of compact RF systems. BST RF MEMS resonators offer great frequency tunability and can be turned on and off by the application of a DC voltage.

Furthermore, a higher overtone frequency response can be excited by selectively patterning the electrodes of the filter. Hence, arrays of resonators that cover a broad

frequency band can be fabricated on a single chip. A band-pass filter that has a small footprint can then be realized by coupling contour-mode resonators mechanically with a small coupling spring. Unlike the commonly available electrically-coupled ladder filters, mechanically-coupled filters occupy a much smaller area.

Through this master's thesis, the design of resonators with metal electrodes that can withstand high temperatures and have multiple release methods will be investigated. Additionally, statistical enhancements of etching thin films will be comprehensively characterized. The feasibility of producing robust band-pass filters for use in the next generation of GPS satellites will be extensively studied.

1.3 Assumptions/Limitations

There are several limitations in this line of thesis work. Many of the decisions made in determining fabrication techniques are based on material availability and available lab equipment. Majority of the fabrication steps were executed in the AFIT Cleanroom Lab; however, due to specific requirements, AFRL Cleanroom Labs were utilized as well.

1.4 Thesis Overview

This thesis is organized into five chapters. The second chapter begins with a literature review of the fundamental principles associated with RF MEMS filters. Chapter three highlights the design and fabrication steps taken to build the RF resonators and filters. Chapter four is a summary of the results gathered from extensive characterization. Finally, chapter five concludes the work accomplished in this paper and discusses potential future work.

II. Literature Review

2.1 Chapter Overview

This chapter provides a short foundation of understanding for the research ideas proposed in later chapters. This chapter also provides a background of the current MEMS (Microelectromechanical Systems) radio frequency filters. MEMS resonators have been extensively examined for filtering applications in wireless communication systems. There has been an emphasis on reducing size, power consumption, and cost of these filter modules.

MEMS filters are designed by electrically or mechanically coupling MEMS resonators. MEMS resonators can be either electrostatically-transduced or piezoelectrically-transduced. Each method of transduction offers its own unique advantages over the other. Electrostatically-transduced resonators offer higher quality factors, but they have very large motional resistances.[5] High motional resistance results in higher losses and less effective resonators. In contrast, piezoelectric resonators offer unique advantages in motional resistance. Piezoelectric resonators have lower electromechanical coupling coefficients, but they also have very low motional resistances.[6]

2.2 Piezoelectricity

Piezoelectric resonators were chosen for this thesis due to their better performance compared to electrostatically-transduced resonators at higher frequencies. Piezoelectric resonators utilized to build filters work well because very high quality factors are not a strict requirement.[7]

Piezoelectricity is defined as the electric charge that accumulates in a certain solid material. Piezoelectric resonators operate on the piezoelectric effect discovered by Pierre and Jacques Curie in the 1880s.[8] The piezoelectric effect is the ability of material to produce an electric field when a certain amount of mechanical stress is applied. The reverse is also true for piezoelectric materials. Mechanical stress can be generated in a material when an electric field is applied. The displacement from an applied electric field in a piezoelectric material can be expressed with mathematical equations. The electrical behavior of the piezoelectric material operating in a linear region can be described by the following equations.[9]

$$D = \varepsilon^S * E + eS \quad (1)$$

$$T = C^E * S - eE \quad (2)$$

D is defined as the electric field displacement, ε is the permittivity of the piezoelectric, E is the electric field strength, S is the strain, T is the stress, C is the stiffness matrix, and e is the piezoelectric coefficient.

2.3 Piezoelectric Resonators

Piezoelectric resonators operate on the innate material property of certain materials known as piezoelectricity. Piezoelectric resonators are typically constructed with a piezoelectric material sandwiched between two metal electrodes, as shown in Figure 1. The resonance mode of the piezoelectric substrate is excited when the frequency of the applied signal matches the resonance frequency of the piezoelectric layer.[7]

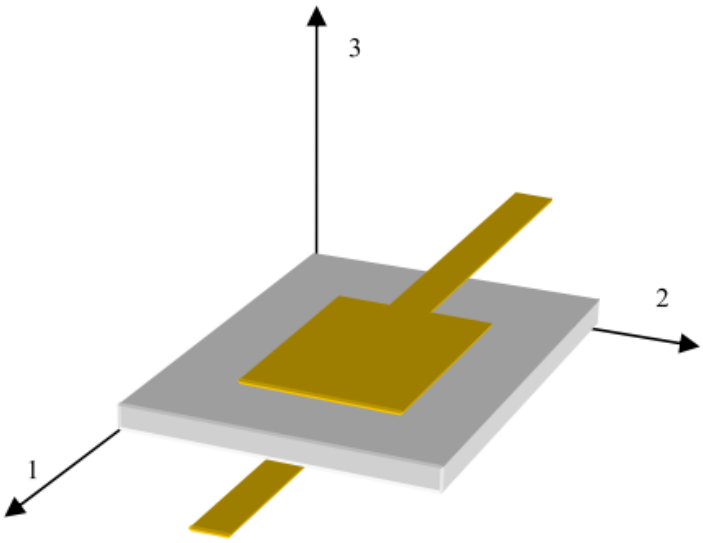

Figure 1: Stack of a piezoelectric substrate sandwiched between two metallic electrodes

Advancements in piezoelectric MEMS resonators have come a long way over the last two decades. There has been a significant industry level push to implement piezoelectric MEMS resonators in various sensors and modules due to their advantages in size, power, cost, and overall efficiency. The range of applications of piezoelectric MEMS resonators can be seen in Figure 2. These piezoelectric resonators can be applied in fingerprint sensors, LiDAR, inertial sensors, infrared sensor, mass sensors, energy harvesters, and most importantly radio frequency communications modules.[10]

For the purposes of this thesis, the focus of piezoelectric MEMS resonators will be placed on their RF applications. Figure 3 depicts a robust application of how multiple piezoelectric resonators can be integrated into one RF module to reduce the size and power consumption of the RF modules.

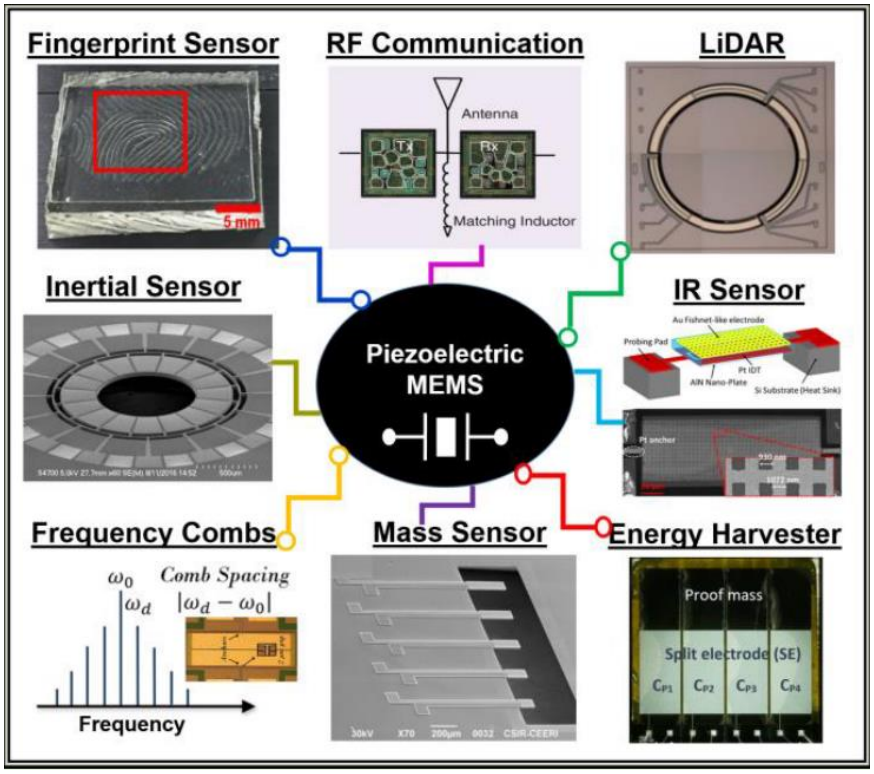

Figure 2: Extensive range of applications for piezoelectric MEMS resonators[10]

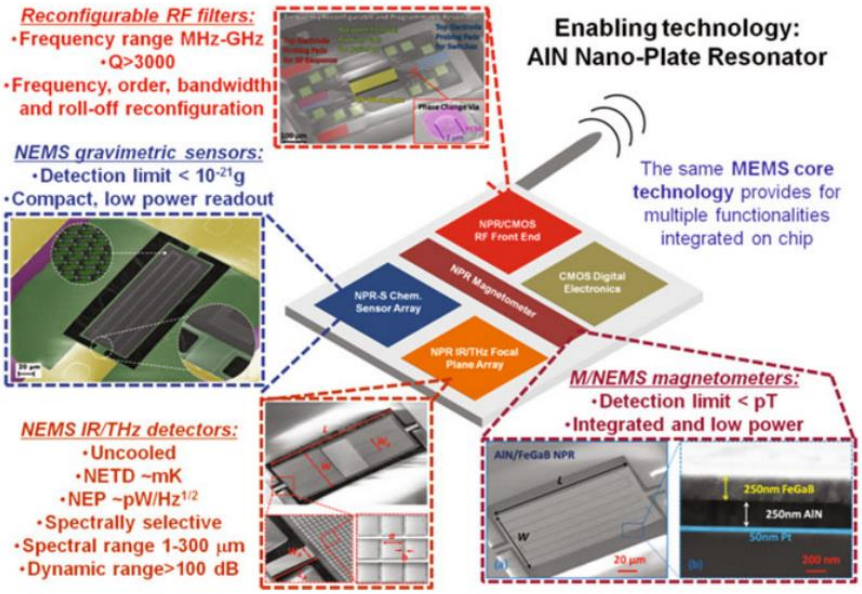

Figure 3: RF sensing platform designed using multiple AlN laterally vibrating piezoelectric resonators[11]

2.4 Zinc Oxide

Zinc oxide is a commonly used piezoelectric material in many thin film applications. ZnO has been implemented in various actuation and sensing devices to include RF piezoelectric MEMS resonators.[12] ZnO offers unique advantages over popular piezoelectric materials used for similar device fabrication. Low deposition temperature, strong bonding, unique semiconducting properties, and a great coupling coefficient makes ZnO a strong candidate for RF MEMS applications.[13][14] In addition to the stated advantages, ZnO is widely considered a green piezoelectric material in contrast to PZT, a lead based piezoelectric.[15] As seen in Figure 4, ZnO is also a robust semiconductor material used to design thin film transistors. System integration of the ZnO resonators and ZnO thin film transistors on the same substrates offers desirables such as: decreased size, increased efficiency, and improved active gain.[16]

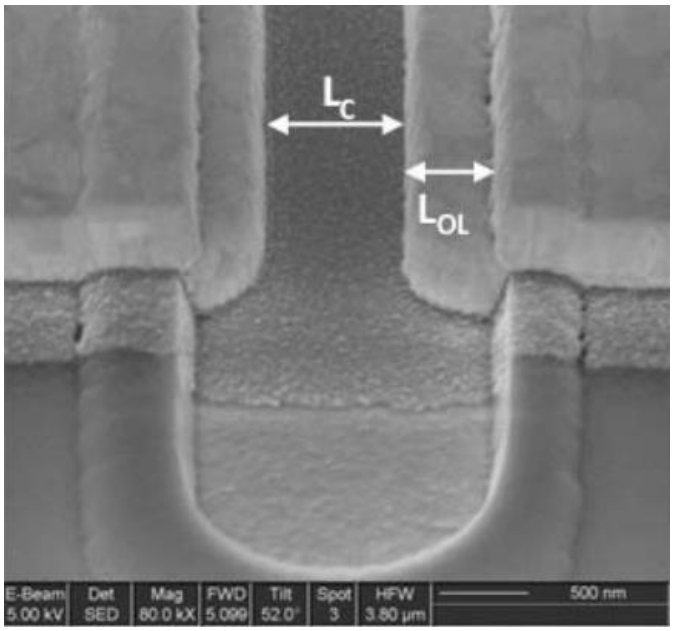

Figure 4: Scanning electron microscope of a zinc oxide thin film transistor compatible with zinc oxide resonators fabrication [16]

2.5 Ferroelectric Barium Strontium Titanate

ZnO is a non-ferroelectric polar material, and it naturally exhibits the piezoelectric effect. In contrast, Barium Strontium Titanate (BST) is a ferroelectric material because it possesses a stable spontaneous polarization that switches in the presence of an electric field. BST thin films do not exhibit acoustic resonances in the absence of a DC field. Once a DC field is applied, the symmetry of the BST crystal is broken and piezoelectricity can be observed. Figure 5 depicts the relationship of ferroelectric materials to piezoelectric materials. Ferroelectric materials are considered to be pyroelectric which also makes ferroelectrics a piezoelectric material. However, the inverse is not true.

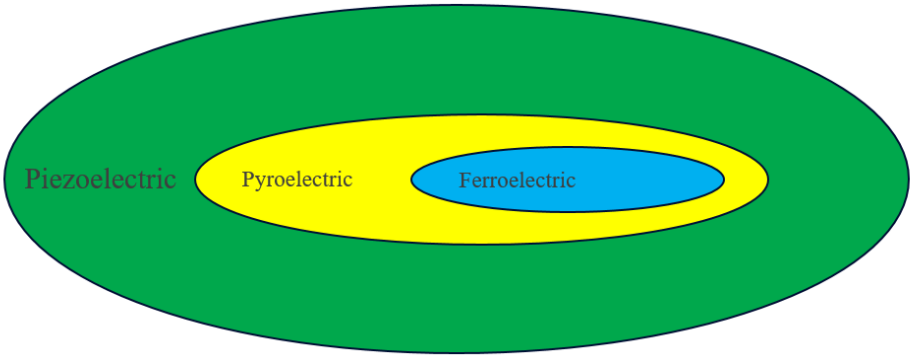

Figure 5: Classification of piezoelectric and ferroelectric materials. Ferroelectric materials are considered as piezoelectric materials but the inverse is not true

In thin film BST, observed piezoelectric effect is associated with the strong electrostrictive effect.[17] Electrostriction is a property of ferroelectric materials, and it describes the strain of a material in the presence of an electric field. Electrostriction can be thought of as DC field induced piezoelectricity.[18] Under the effect of an applied DC

field, the effective piezoelectricity in BST can be expressed by the following equations.[19]

$$d_{31} = \frac{D_{31}}{T - T_d} \quad (3)$$

$$g_{31} = \frac{G_{31}}{\left(T - T_g\right)^2} \quad (4)$$

$$d_{31}^{*} = d_{31} + 2g_{31}E_3 \quad (5)$$

The effective piezoelectric constant includes the piezoelectric (d_{31}) and electrostrictive (g_{31}) components. The value of d_{31} for BST has been calculated at -9.6×10^{-12} C/N.[20]

Application of a DC field across a thin film of BST displaces the center titanium ion the crystal lattice. The displacement of the center titanium ion polarizes the ferroelectric thin film which causes electric field induced piezoelectricity. The distinction between naturally occurring piezoelectricity and electric field induced piezoelectricity, electrostriction, can be seen in Figure 6.[21]

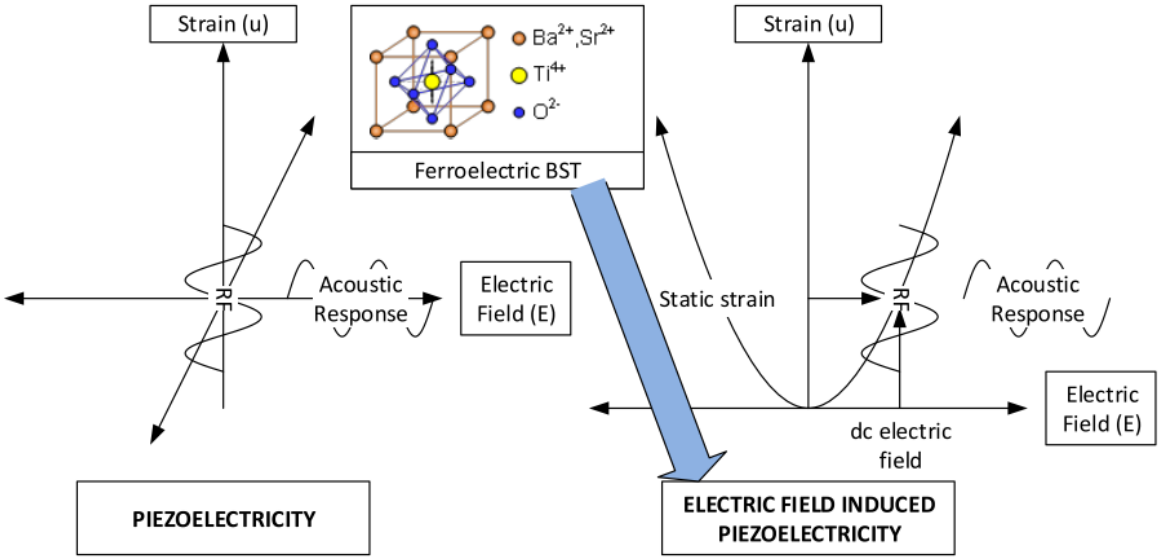

Figure 6: Strain vs Electric Field for Piezoelectricity and Electrostriction [21]

2.6 Electrode Material

The metals used as the electrodes for the resonators are carefully chosen based on their unique properties. The resonators built in this thesis have potential to be utilized as filters in the next generation of GPS satellites that will orbit planets with extremely high temperatures, such as Venus. Consequently, the electrode materials chosen for the design of the resonators must have high melting temperatures that can withstand the near 500°C atmospheric temperatures of Venus. Therefore, tungsten is the metal of choice for the ZnO resonators, and platinum is used for the BST resonators. The melting point for tungsten 3,410°C[22], and platinum has a lower melting point of 1,769°C.[23]

In addition to the melting point advantage, tungsten is a relatively easy metal to sputter and to etch using reactive ion etching (RIE). Tungsten has a high acoustic impedance which improves the effective coupling coefficient.[24]

2.7 Resonator Mechanical Modeling

A piezoelectric resonator is free standing structure that can be excited into vibrations when an alternating electric field at the structure's resonant frequency is applied.[25] The piezoelectric resonator, therefore, can be represented by a simple mass-damper-spring system as shown in Figure 7.

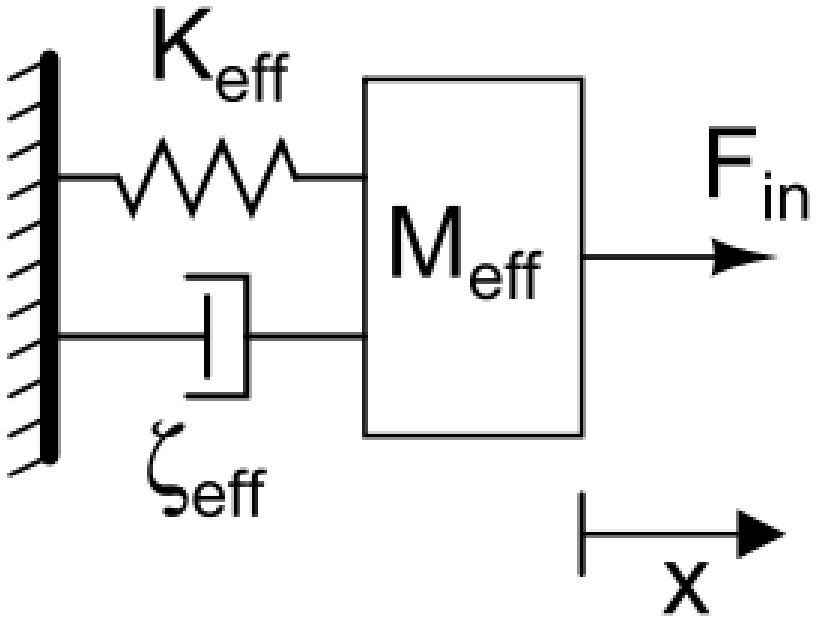

Figure 7: A mass-damper-spring system representation of a mechanical resonator

The effective mass of can be defined by dividing the total kinetic energy of the resonator by half of the velocity. Therefore, the natural resonance frequency of the resonator can be defined by equation 6.

$$f = \frac{A}{B}\sqrt{\frac{E}{\rho}} = \frac{1}{2\pi}\sqrt{\frac{K_{eff}}{M_{eff}}} \quad (6)$$

In equation 6, A is a unit less number, B is a unit of length, E is the Young's modulus, and ρ is density of the material. Zeta (ζ) is the damping coefficient that measures the energy loss of spring-mass-damper system, and it can be defined based on the quality factor (Q) of the resonator.

$$\zeta = \frac{2\pi f M_{eff}}{Q} \tag{7}$$

For a resonator bar with a width, W, resonating in the extensional mode, the resonant frequency can be defined using equation 8.

$$f = \frac{n}{2W}\sqrt{\frac{E}{\rho}} \tag{8}$$

From equation 8, effective mass can be defined using equation 9.

$$M_{eff} = \frac{\rho AW}{2} \tag{9}$$

Thus, the effective stiffness of the system can be defined using equation 10.[7]

$$K_{eff} = \frac{n^2\pi^2 AE}{2W} \tag{10}$$

2.8 Resonator Equivalent Electrical Modeling

A piezoelectric resonator can also be represented by the Butterworth-Van Dyke (BVD) model.[26] The basic BVD model has a capacitor in parallel connected to a resistor, capacitor, and inductor in series as shown in Figure 8. R_m is the motional resistance, C_m is the motional capacitance, L_m is the motional inductance, and C_o is the static capacitance of the piezoelectric resonator. The analogous relationship between the electrical and mechanical properties of the resonator allows for the simulation and modeling in the electrical domain. Using the equations for effective mass and effective spring constant for section 2.7, the electrical properties of the properties of the equivalent electrical model can be calculated.

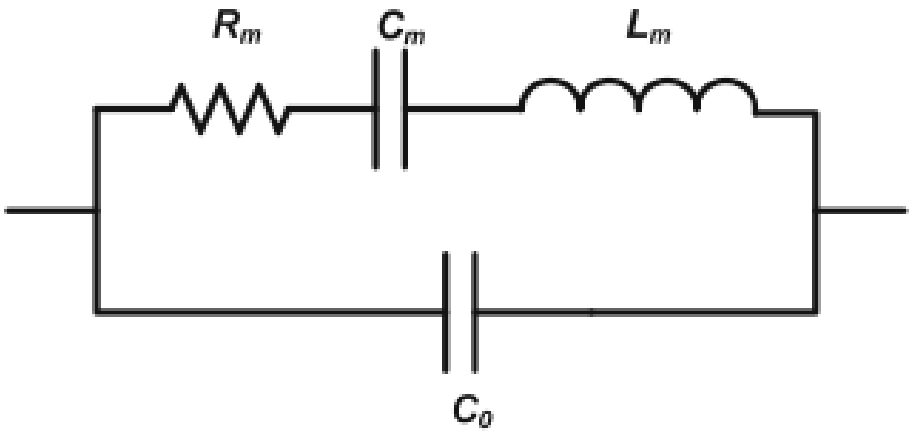

Figure 8: Piezoelectric resonator equivalent electrical circuit used for modeling and simulation

The values of R_m, C_m, L_m, and C_o for piezoelectric resonators have been extensively calculated in previous works.[27] The small signal electrical equivalent impedances for a piezoelectric resonator operating in the fundamental mode can be calculated using the equations below.

$$R_m = \frac{\sqrt{K_{eff} M_{eff}}}{Q\eta^2} \tag{11}$$

$$C_m = \frac{\eta^2}{K_{eff}} \tag{12}$$

$$L_m = \frac{M_{eff}}{\eta^2} \tag{13}$$

M_{eff} is effective mass of the resonator body, and K_{eff} is the effective spring constant of the resonator. The efficiency of the electromechanical transduction is represented by the symbol η, known as eta. Eta is the electromechanical coupling constant.

2.9 Modes of Operation

The resonators used in this thesis will be bar resonators operating in the width extensional mode (WEM) and length extensional mode (LEM). The resonator's frequency in WEM is determined by the width of the bar. This can be seen in the equation below.

$$f = \frac{n}{2W}\sqrt{\frac{E}{\rho}} \tag{14}$$

The variable n represents the mode number of the resonator, W is the width of the resonator, E is the young's modulus resonator material, and ρ is the density of resonator material. The finite elemental analysis (FEA) of the WEM mode of operation can be seen in Figure 9 below. The blue areas of the FEA figure indicate zero displacement because that is the location of the anchors on the resonator body. The red area indicates the maximum area of displacement for the WEM mode of operation. The resonator's anchors are methodically placed in the blue regions to minimize losses due to the anchors.

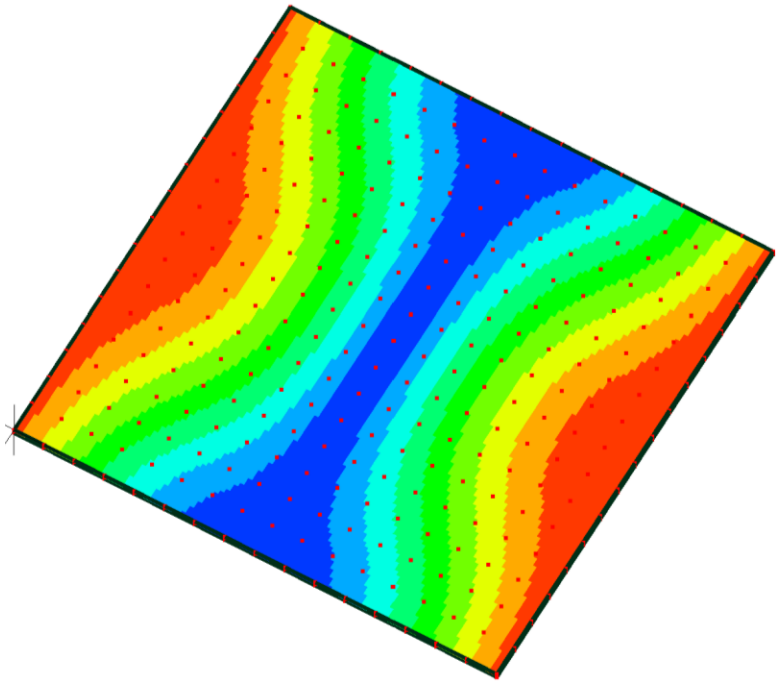

(a)

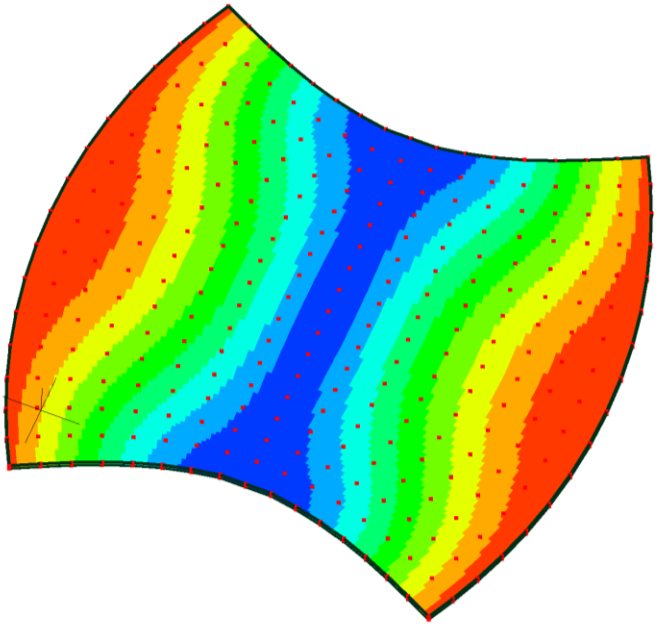

(b)

Figure 9: First-order width extensional resonance mode of a contour mode resonator simulated in Mecway

Similarly, the resonator's frequency in LEM is determined by the length of the bar. This can be seen in the equation below.

$$f = \frac{n}{2L}\sqrt{\frac{E}{\rho}} \tag{15}$$

The variable n represents the mode number of the resonator, L is the length of the resonator, E is the young's modulus resonator material, and ρ is the density of resonator material. The FEA of the LEM mode of operation can be seen in the Figure 10. Again, the color red indicates the maximum area of displacement, and the blue identifies zero displacement. The blue region in the FEA figure is the location of the anchors on the resonator body. The anchors are strategic placed in that center location to minimize anchor loss.

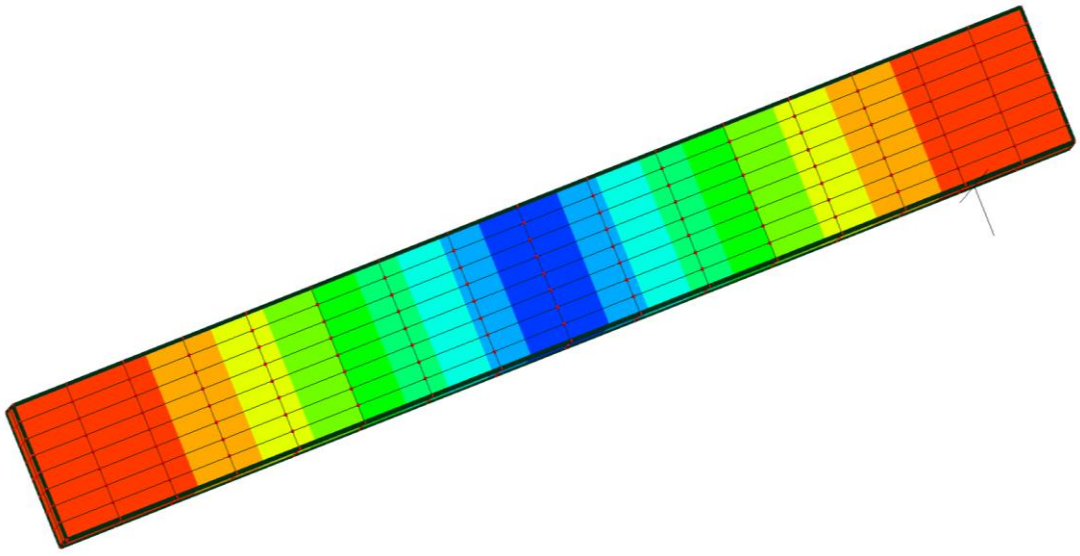

Figure 10: First-order length extensional resonance mode of a contour mode resonator simulated in Mecway

2.10 Filters as Mechanically Coupled Resonators

Over the past couple of years, demand for highly integrated filters operating in multiple bands has exponentially increased. Band-pass filters are an essential part of wireless communications, and the next generation of wireless standards, such as 5G, will rely heavily on the advantages of piezoelectric MEMS resonators for implementation. Figure 11 shows projections from a leading company in 5G operations on how piezoelectric bulk acoustic wave resonators will aid RF filtering in new enabling technologies.

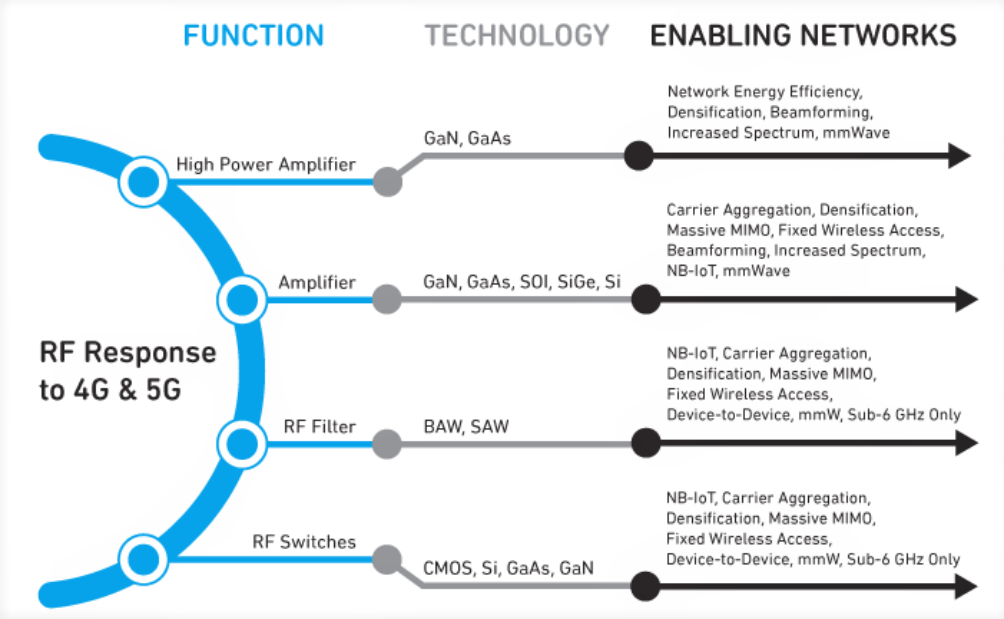

Figure 11: Use of piezoelectric MEMS filters in 5G technologies [28]

Therefore, the resonators designed in this thesis can be coupled together to produce quality RF filters. Traditionally, resonators are electrically coupled together to form filter topologies, but the filters designed in this thesis are mechanically coupled together. An example of a mechanically coupled filter can be seen in Figure 12.[29]

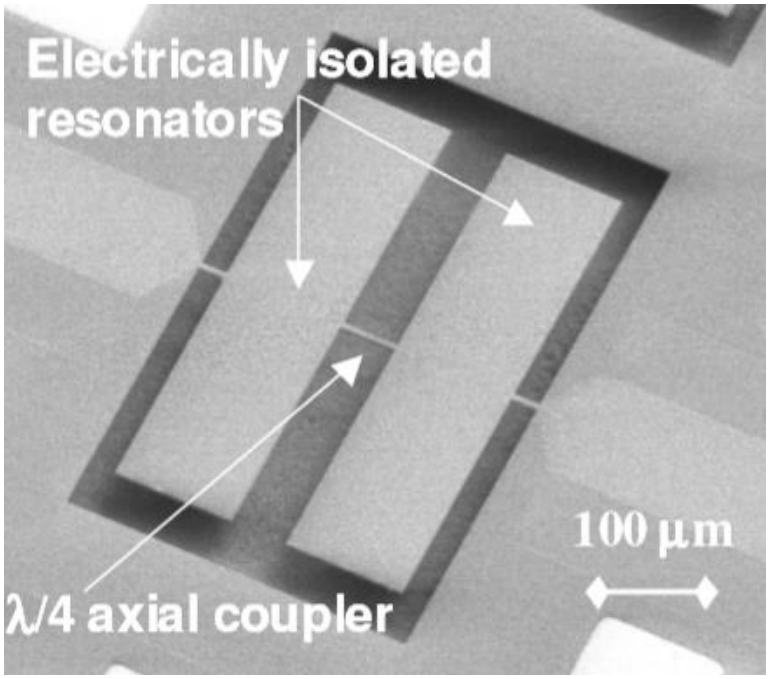

Figure 12: Piezoelectric MEMS RF resonators mechanically coupled together to form a filter [29]

Mechanically coupled resonators offer a few advantages over electrically coupled resonators. Most significantly, mechanically coupled resonators provide a smaller footprint.[30] Decreased size is a major innovation factor in wireless communication applications. Along with smaller size, mechanically coupled resonators do not face the bandwidth limitations observed in electrically coupled resonators.[31] A depiction of generic band-pass filter can be seen in Figure 13.

Piezoelectric resonators have been coupled together and have shown filtering capabilities in the ultra-high frequency range. ZnO and BST are the two piezoelectric materials that will be studied in this thesis paper. These filters need to be designed with insertion loss in mind. Piezoelectric resonators allow the creation of filters that exhibit low insertion loss and high electromechanical coupling of the resonators. [1]

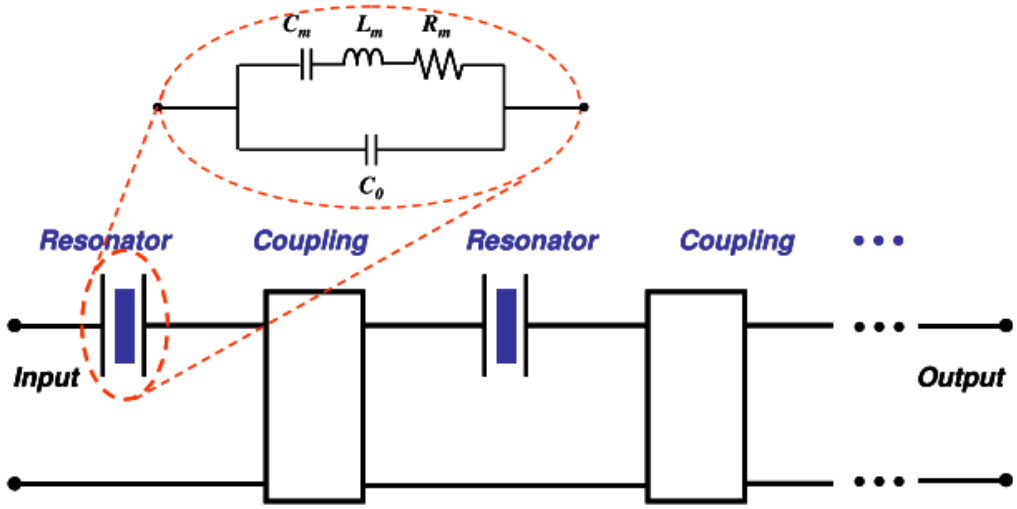

Figure 13: Generic band-pass filter topology for mechanically coupled resonators

2.11 Quality Factor

The quality factor (Q) of a resonator is a measurement of energy loss. Q is viewed as a parameter that expresses the degree of energy dissipation in a resonator or filter.[32] The quality factor is typically defined as stated in equation 16.

$$Q = 2\pi \frac{Energy\ Stored\ per\ Cycle}{Energy\ Dissipated\ per\ Cycle} \tag{16}$$

In the operation of these MEMS resonators and filters, energy is converted from one form to another multiple times. The energy flow of piezoelectric transduction can be seen in Figure 14.[11]

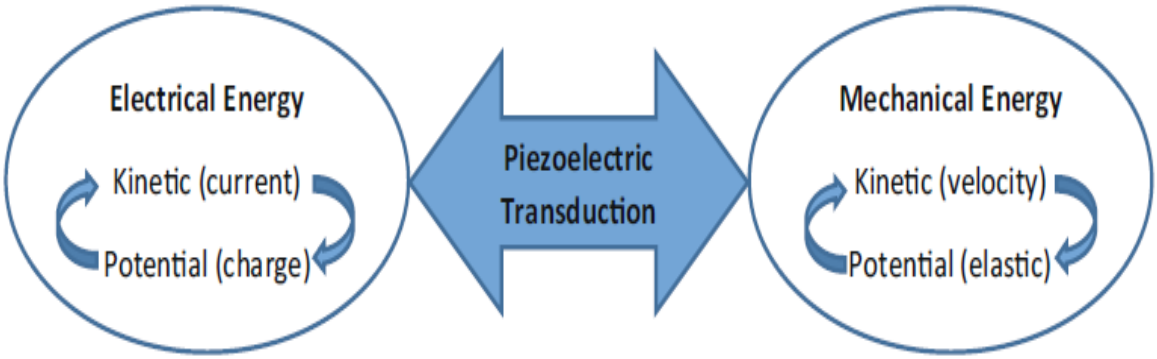

Figure 14: Energy flow in a piezoelectric resonator illustrating the piezoelectric effect[11]

A higher quality factor is a desired feature in a resonator. A high quality factor results in better performing filter due to the lower insertion loss and improved signal transmission. The quality factor of a resonator can also be defined based on its frequency response as seen in equation 17.

$$Q = \frac{f_o}{BW_{-3dB}} \tag{17}$$

BW is the -3dB bandwidth near the resonant frequency of the resonator.[33] A sharper peak is desired from the frequency response of a resonator which indicates a higher quality factor and minimal losses. An illustration of various quality factors compared can be seen in Figure 15 below.

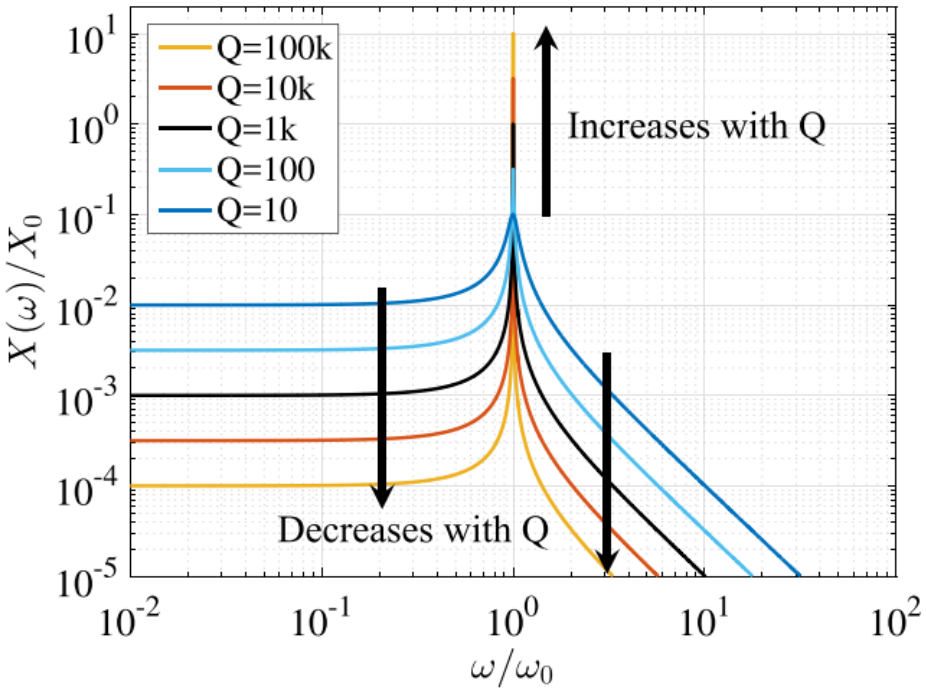

Figure 15: Illustration of frequency responses with different quality factors

The overall quality factor is a summation of various energy loss parameters. The mathematical breakdown of the quality factor can be seen in equation 12.[34]

$$\frac{1}{Q} = \frac{1}{Q_{Air}} + \frac{1}{Q_{TED}} + \frac{1}{Q_{Anchor}} + \frac{1}{Q_{Surface}} + \frac{1}{Q_{Phonon}} + \frac{1}{Q_{Others}} \qquad (18)$$

Q_{Air} is the damping due to air. Q_{TED} is known as thermoelastic dissipation, and it represents the intrinsic damping due thermal and elastic deformation fields around the resonator.[35] Q_{Anchor} is damping due anchor loss. Anchor loss is best described as the lost vibrational energy of a resonator to the foundation substrate through the resonator's supporting beams.[36] $Q_{Surface}$ is damping caused by damages and foreign particles on the

surface of the resonator body. Q_{Phonon} is energy loss through phonon-phonon interactions. This case of energy loss happens as a result of disruptions in the local equilibrium of phonons caused by the stress and strain in the resonator.[37]

2.12 Electromechanical Coupling Factor

Along with quality factor, the electromechanical coupling factor of a resonator is a quantitative approach of measuring the efficiency. The electromechanical coupling factor, K^2, represents the energy conversion efficiency of the resonator.[38] Table 1 identifies the K^2 of commonly utilized piezoelectric materials. ZnO possess a higher couple factor compared to other materials still widely used today. PZT has a coupling factor almost three times larger than ZnO, but PZT is no longer considered an environmentally friendly material.[39] The lead component in PZT makes it a generally toxic material, so PZT cannot be processed in a standard CMOS cleanroom. Additionally, monolithic integration with transistors is difficult to perform using PZT.

Table 1: Common Electromechanical Coupling Factors

Material	**Quartz**	**AlN**	**ZnO**	**PZT**
K^2 (%)	0.86	6.5	8.5	23

III. Methodology

3.1 Chapter Overview

The purpose of this chapter is to illustrate the steps taken to fabricate the RF MEMS resonators and filters. This chapter also includes the reasons behind the decisions made in the design of the RF filters, and the assumptions and limitations faced in the fabrication process. The various materials used in the design of the resonators require specialized attention in order to process. Etching ZnO versus etching BST is an entirely different method, so each material processing step has to be carefully characterized and verified.

The fabrication of the MEMS resonators and filters requires a multi mask process. The resonators are first designed in a layout software called L-Edit. Once the resonators are built in L-Edit, the design is broken into appropriate layers. Each L-Edit layer represents a fabrication step in the processing of the resonators. The individual layers are converted to the appropriate file format and loaded into the Heidelberg μPG 101 mask writer. A segment of all three layers of the mask as displayed in L-Edit can be seen in Figure 16. Properly printed masks are key to a successful lithography process. The lithography process is used to prepare the individual layers for material processing. The overall fabrication process is straightforward, but the true challenge arises in the individual material processing steps. This chapter will expand on the challenges faced in each step.

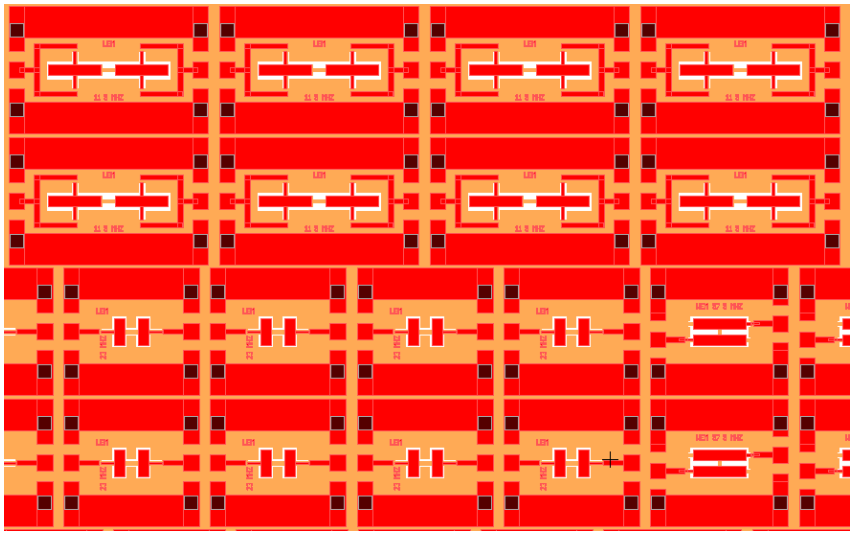

Figure 16: Layout editing software for the design of RF MEMS piezoelectric resonators

3.2 Fabrication Process of Zinc Oxide Resonators

The ZnO resonators designed in this thesis were developed using two different processes. The first design process has the resonators built on a silicon dioxide substrate, and the second design process has the resonators built on a silicon substrate. Using two different base substrates allows for two different release methods of the resonators. Resonators built on silicon dioxide are released using vapor hydrogen fluoride and, resonators built on silicon substrates are released using xenon difluoride. The two design processes are very similar, but the main difference is that in the silicon substrate design the bottom tungsten electrode has a thin 100 nm layer of silicon dioxide grown underneath. The silicon substrate design method also requires a fourth mask to protect the tungsten during the xenon difluoride release process. The reasons for the extra layers will be further explained later in the chapter.

Figure 17 shows the step by step fabrication process for the silicon dioxide substrate ZnO resonator design process. The resonators in this design will be released using vapor hydrofluoric acid (HF). Each of the fabrication steps will be described in further detail throughout the chapter.

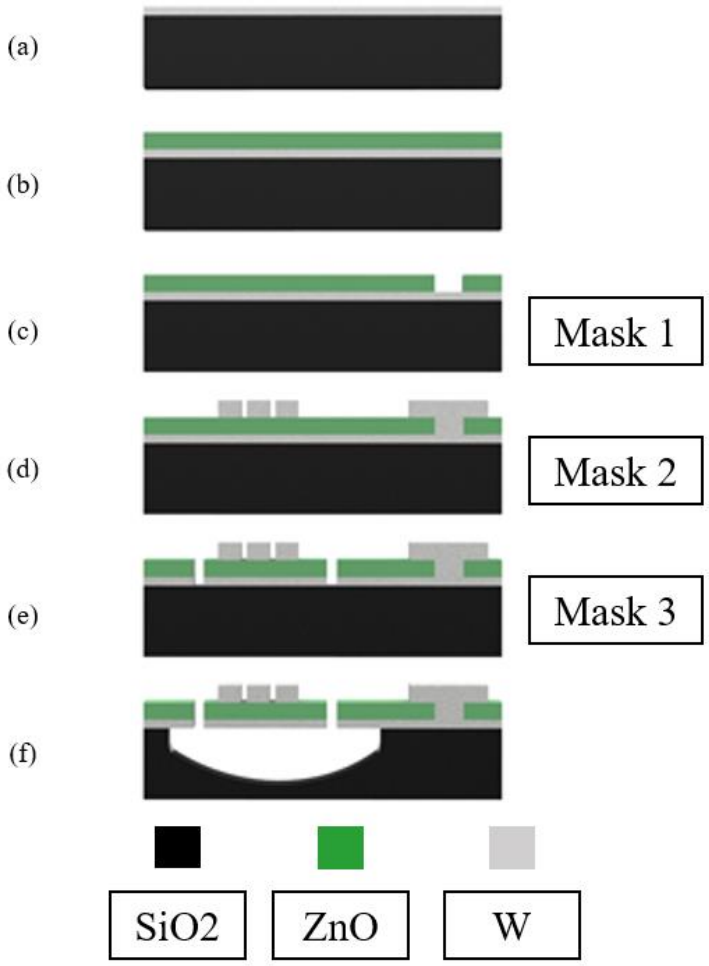

Figure 17: Fabrication process steps of piezoelectric ZnO resonators built on silicon dioxide wafers. (a) 100 nm of bottom electrode tungsten deposition. (b) 500 nm ZnO deposition. (c) Mask 1 patterning of ZnO. (d) Deposition and patterning of top electrode tungsten with mask 2. (e) Mask 3 patterning of resonator shape and etching of bottom electrode. (f) Isotropic release of ZnO resonators using vapor HF.

The fabrication process begins with a thin film deposition of 100 nm of tungsten onto a silicon dioxide wafer. The tungsten is deposited using AFIT's Kurt Lesker Sputtering system. Following the tungsten deposition, 500 nm of ZnO is deposited using AFRL's Neocera Pioneer 180 Pulsed Laser Deposition system. The parameters for ZnO deposition can be seen in Table 2.

Table 2: ZnO Sputtering Parameters

Parameter	**Value**
Base Pressure	$2.67 \text{ x} 10^{-5}$ Pa
Laser	KrF Excimer
Wavelength	248 nm
Pulse Duration	10 ns
Frequency	30Hz
Energy Density	2.6 J/cm^2
Deposition Rate	0.25 nm/s

3.2.1 Zinc Oxide Wet Etch Solutions

The first mask fabrication step calls for etching of the 500 nm ZnO layer to expose the bottom electrode. The first attempts to etch ZnO resulted in extremely unsuccessful results. ARFL's reactive ion etching process was used to etch ZnO samples. The reactive ion etching process largely etched away the protective photoresist layer instead of the ZnO. For the fabrication of the resonators, the photoresist needs to survive the etch process. The alternative to a dry etch is a wet etch process. Wet etching a wafer means submerging the wafer in a known solution that will erode the unprotected ZnO

areas. The literature suggests many different solutions to wet etch ZnO such as: hydrogen peroxide, sulfuric acid, phosphoric acid, hydrochloric acid, and ammonium chloride.[40][41][42] In this thesis research, each ZnO wet etch solution is characterized and ranked on overall effectiveness.

Hydrogen peroxide was the first solution tested to wet etch ZnO. Unfortunately, hydrogen peroxide did not produce the best results, and it was in short supply in the lab. For those reasons, hydrogen peroxide was rejected and sulfuric acid was tested next. Sulfuric acid successfully etched ZnO, but it produced wildly inconsistent results. The next two wet etch chemistries utilized to etch ZnO were phosphoric acid and hydrochloric acid. Phosphoric acid and hydrochloric acid showed potential for success, so they were further studied. Their etch rates were carefully characterized as shown in Table 3 and Table 4.

Table 3: ZnO Etch Rate using 0.00125M Phosphoric Acid

Time (min)	**Avg ZnO Etch Rate (um/min)**
1	0.0177
2.25	0.0083
8.5	0.0228

Table 4: ZnO Etch Rate using 0.00125M Hydrochloric Acid

Time (min)	Avg ZnO Etch Rate (um/min)
1.5	0.121
2	0.108
3	0.168
4	0.078
5	0.107
6	0.153

The results of the phosphoric acid and hydrochloric acid produced an average etch rate of 16 nm/min and 123 nm/min, respectively. The results of the phosphoric acid etch were immediately dismissed due to inconclusive test runs. The etch rate was slow, and it was extremely difficult to reproduce consistent results. The hydrochloric acid wet etch displayed the best results up to this point. Figure 18 and 19 show a scanning electron microscope (SEM) and microscope image of the hydrochloric wet etch.

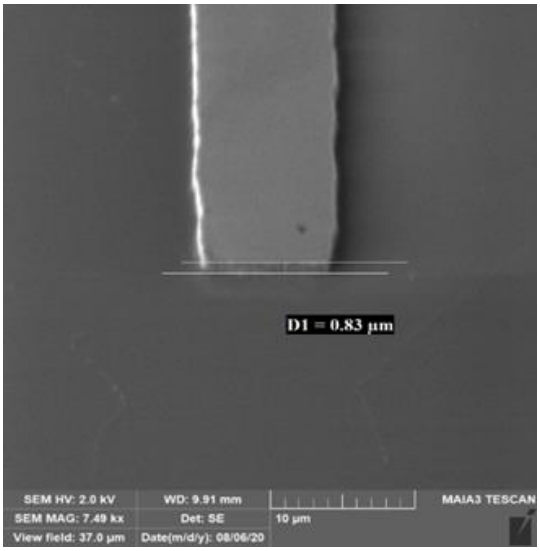

Figure 18: Scanning electron microscope image of hydrochloric wet etch showing complete etch of 800 nm ZnO test chip

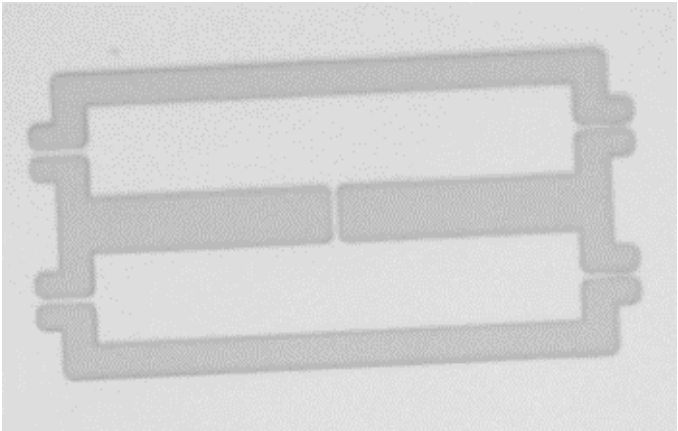

Figure 19: Optical microscope image of hydrochloric wet etch showing thinned out tethers from significant lateral etching

However, the hydrochloric acid wet etch still did not exhibit entirely desirable characteristics. The hydrochloric wet etch had significant lateral etching and thinned out the anchors of the resonators or completely destroyed them. The etch results seemed

inconsistent at best. The etch rate was largely affected by the agitation level of the solution. Unfortunately, agitation is an extremely difficult parameter to quantify.

The overall best wet etch of ZnO was accomplished using ammonium chloride (NH_4Cl). Unlike the acids stated above, ammonium chloride is packaged as a white powder. The ammonium chloride wet etch solution is created by mixing the powder with water. An extensive ammonium chloride wet etch study was conducted to discover the optimum percent concentration to etch 500 nm of ZnO.

3.2.1.1 Ammonium Chloride Wet Etch Study

Ammonium chloride was determined to be the best wet etch solution for patterning ZnO; however, the current research did not offer concrete results on the expected etch rates. The inconsistency of current research regarding wet etching ZnO with ammonium chloride inspired a thorough wet etch study.

The study consists of a statistical analysis on the etch rate of ZnO by an ammonium chloride solution. In this study, 14 ZnO chips were etched using various concentrations of ammonium chloride and various etch times. The percent weight concentrations of ammonium chloride used are 5%, 10%, 15%, and 20%. The chips used in the etch study were made up of 500 nm of ZnO on 100 nm of aluminum on a silicon substrate. The ZnO chips were coated with S1818 photoresist and patterned with 1 mm squares. Using a profilometer, the depth of each square was measured after developing the photoresist, after etching in the ammonium chloride solution, and finally after removing the photoresist. Measuring the depth at multiple points helped determine the etch rate of the ZnO, and the etch rate of the S1818 photoresist. Knowing the etch rate of

the photoresist and etch rate of ZnO in ammonium chloride highlights the selectivity of the etchant. In the case of this study, high selectivity is desirable. The measured etch rates for different concentrations of ammonium chloride can be seen in Figure 20. For the case of the resonators in this thesis, a 10% weight concentration of ammonium chloride was used for etching the ZnO layer.

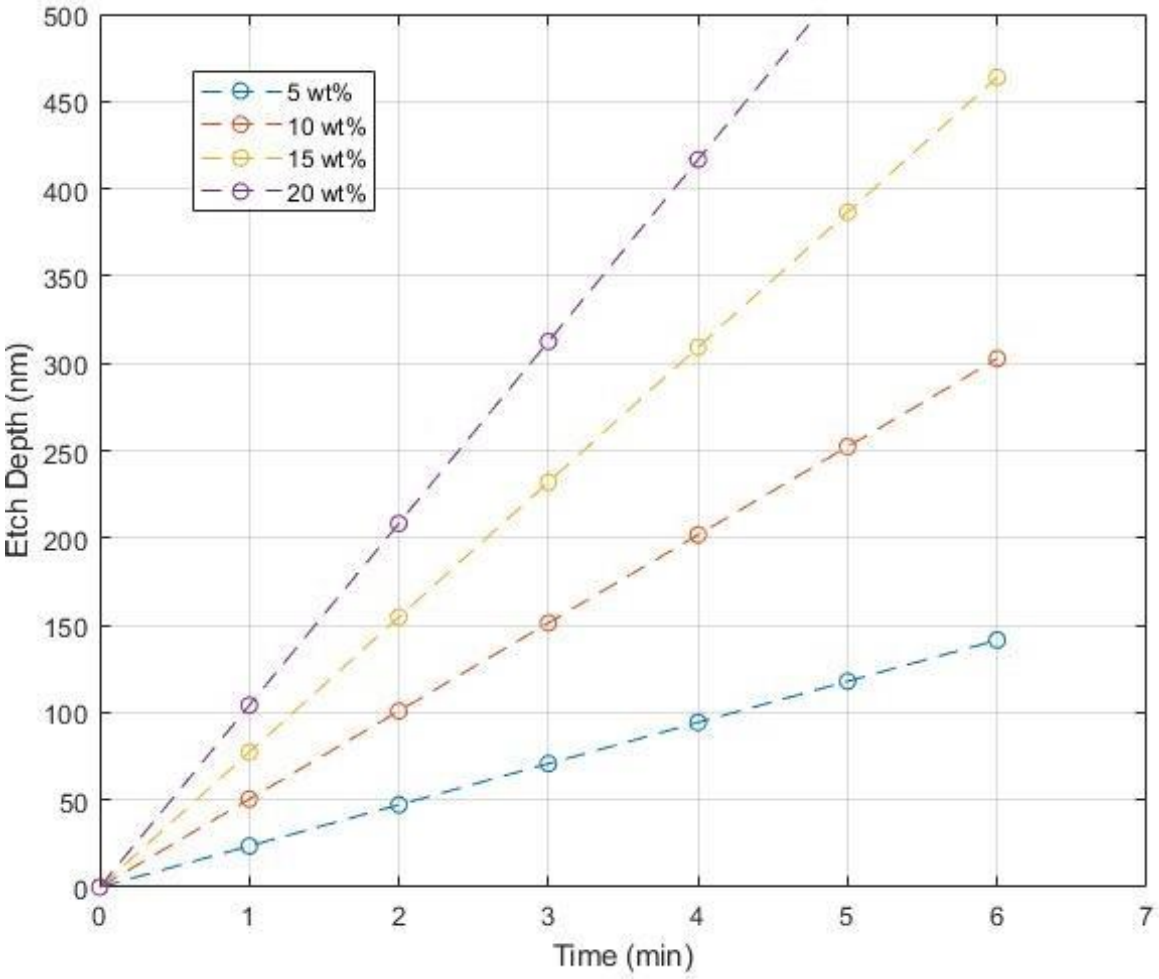

Figure 20: Etch depth vs time for 5%, 10%, 15%, 20% NH_4Cl concentrations from statistical ZnO wet etch study

An optical microscope image of the 1 mm squares on the can be seen in Figure 21. The ZnO is partially etched in some of the squares and fully etched in other squares. A more complete etch of the ZnO in each square appears less cloudy.

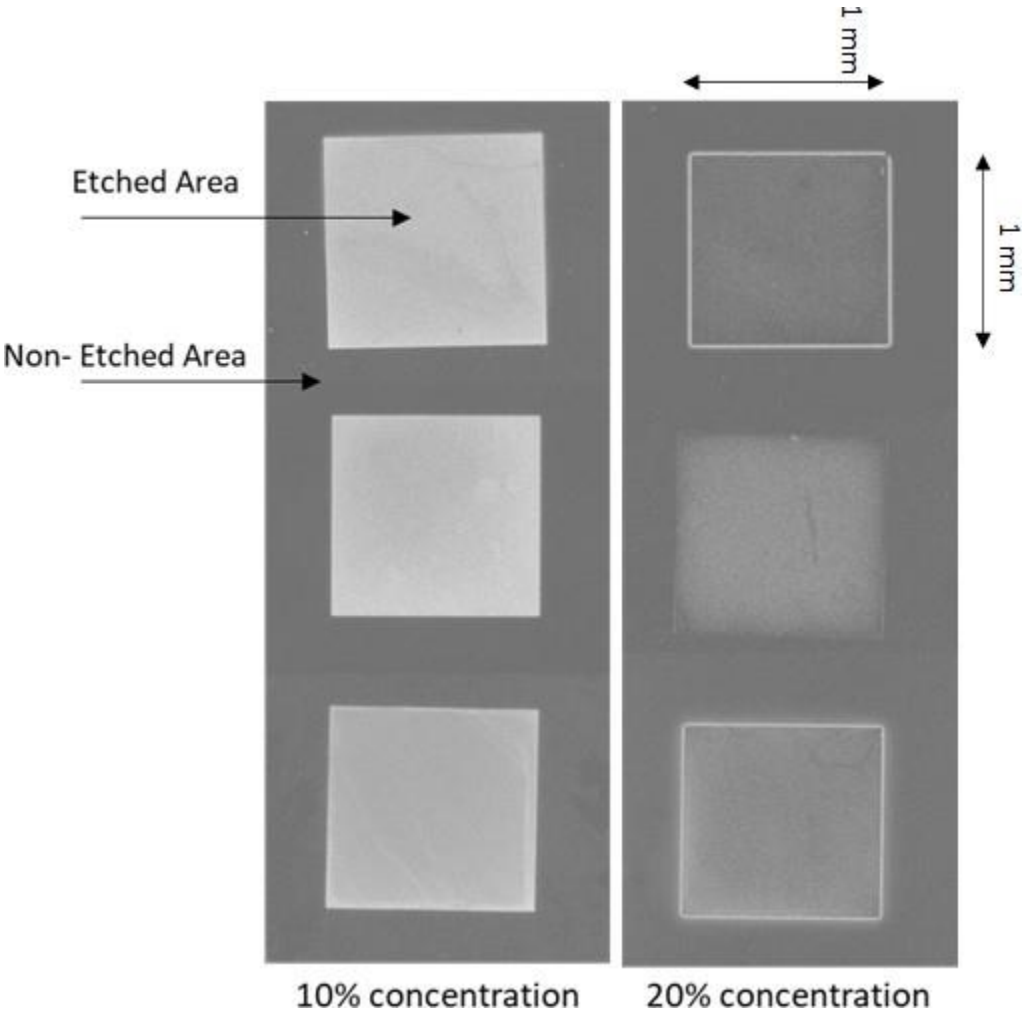

Figure 21: Optical microscope images of NH_4Cl etch results from statistical ZnO wet etch study

The SEM images in Figure 22 show the cross section etch profile of the ZnO squares. The cross sectional images highlight the minimal lateral etch caused by the ammonium chloride.

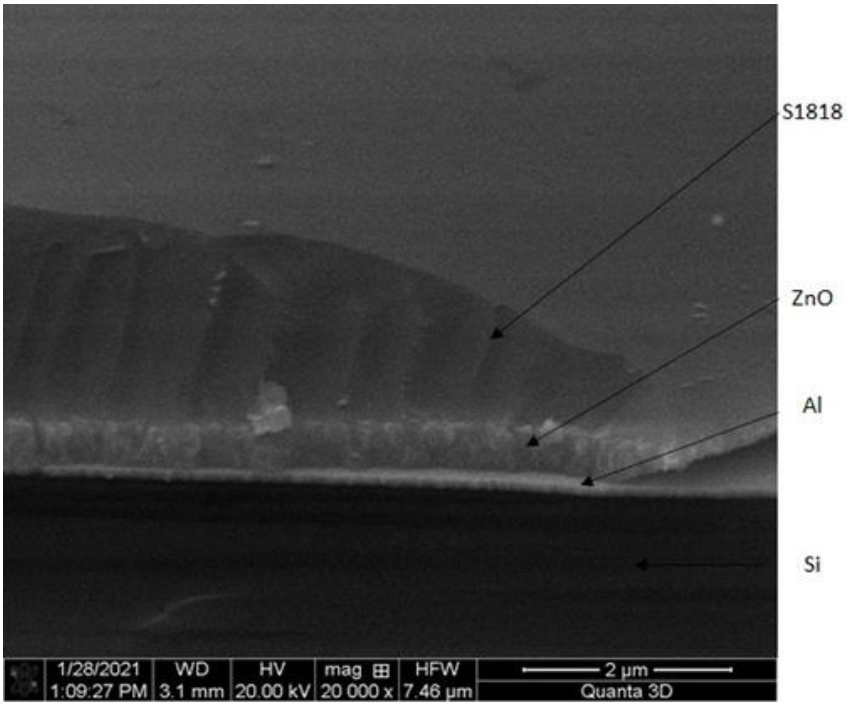

(a)

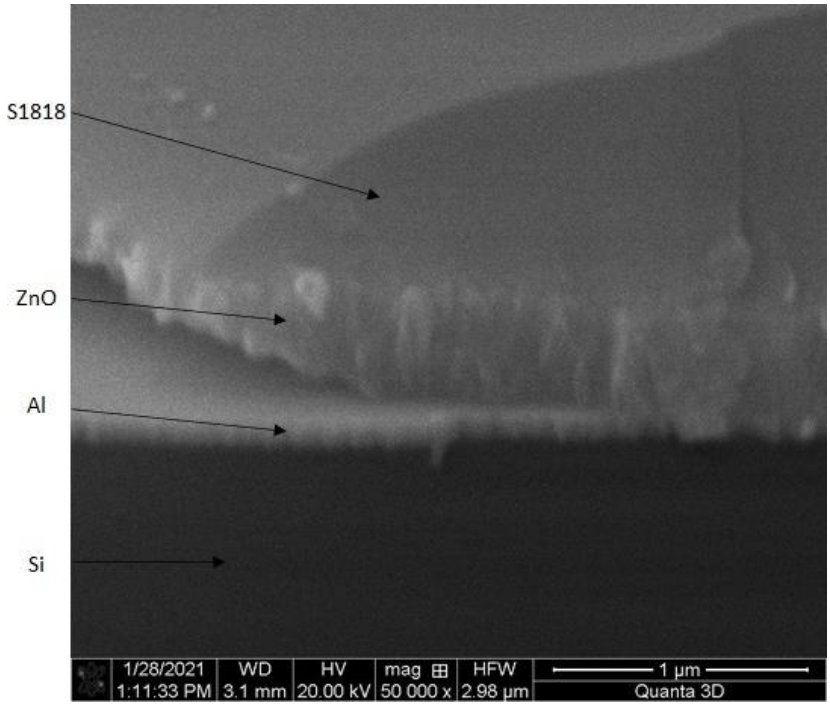

(b)

Figure 22: SEM images of etch profiles from statistical ZnO wet etch study

3.2.2 Tungsten Sputter Deposition

The next step in the fabrication process is the deposition of the top metal electrode. Tungsten is the metal of choice because of its extremely high metaling point and availability in the lab. The Kurt J Lesker Lab 18 sputter deposition system is used to deposit 100 nm of tungsten. The sputter deposition system provides known recipes that offer approximate deposition rates. However, the given deposition recipe was still vetted to ensure the proper deposition of 100 nm of tungsten. The recipe used for tungsten sputtering can be seen in Table 5.

Table 5: Tungsten Deposition Recipe

Parameter	**Value**
Ignition pressure	10
Rotation speed	5
Power	100
Burn in	10
Run pressure	8
Deposition time	1200
Quoted Dep Rate	5.7 nm/min
Measured Dep Rate	6.7 nm/min

3.2.3 Reactive Ion Etching of Tungsten Electrode

The top tungsten electrode has to be selectively etched to form the necessary patterns for proper device operation. Reactive ion etching (RIE) is a highly effective method for patterning metal thin films. The physical ion bombardment, combined with the chemical breakdown, offers reliable etching of a thin film of tungsten. During a RIE process, the chemical breakdown of the target material occurs based on the etching gas utilized. Selecting a specific gas or combination of gases is known as an etch recipe. In this thesis, two different etch recipes for tungsten RIE were studied.

Oxygen and sulfur hexafluoride were the two gases used in the first etch recipe.[43] The remaining parameters were tweaked in order to find the optimal etch rate. Table 6 lists the unique modifications to the first etch recipe. The best etch rate and most consistent results were seen through the last test in table 6. The final parameters produced an etch rate of approximately 3 nm/min.

Table 6: Tungsten Etch Rate with SF_6 and O_2

SF_6 Flow Rate (sccm)	**O_2 Flow Rate (sccm)**	**Pressure (mTorr)**	**ICP (Watts)**	**RIE (Watts)**	**Time (s)**	**Average etch rate (nm/sec)**
20	3	30	350	25	60	over-etch
20	3	30	350	25	6	over-etch
20	3	30	100	10	30	130
10	3	30	100	10	30	3.5
10	3	30	100	10	15	1.8
10	3	30	75	10	30	3.0

The second recipe used to etch tungsten is accomplished using only sulfur hexafluoride. The sulfur hexafluoride etch recipe produced impressive results initially and did not require multiple test variations. The observed etch results were consistent and easily reproducible. The RIE parameters for the sulfur hexafluoride etch can be seen in Table 7. 17 nm/sec is a desirable etch rate that allows the etching of 100 nm of tungsten in approximately 60 seconds.

The results of the tungsten RIE runs were extremely anisotropic. There was no evidence of lateral etching caused to the top electrode. This property of RIE makes it a more desirable etching mechanism when compared to wet etching. Wet etching solutions can be notorious for producing unintended lateral etches.

Table 7: Tungsten Etch Rate with SF_6

SF_6 Flow Rate (sccm)	**Pressure (mTorr)**	**ICP (Watts)**	**RIE (Watts)**	**Time (s)**	**Average etch rate (nm/sec)**
40	110	0	140	60	17

3.2.4 Vapor Hydrogen Fluoride Etch Release for Zinc Oxide Resonators

Following the RIE of the top metal film, the third mask lithography step is accomplished. As seen in Figure 17, the third mask is used to wet etch 500 nm of ZnO using ammonium chloride and RIE of the bottom tungsten electrode. Removing those two layers exposes the silicon dioxide base layer. In order to release the resonators and filters, the silicon dioxide base layer needs to be selectively etched away. Vapor HF is an effective etchant for silicon dioxide.[44] The recipe used for the vapor HF etch can be seen in Table 8.

Table 8: Vapor HF Release Recipe

Parameter	**Value**
Preloaded Recipe No.	4
No. of Cycles	6
Estimate etch	0.63 µm/min

3.2.5 Xenon Difluoride Etch Release for Zinc Oxide Resonators

As stated in the beginning of this chapter, the ZnO resonators were designed using two different processes. The second design process adds a thin layer of silicon dioxide under the bottom electrode and uses silicon as the substrate as seen in Figure 23. The thin 100 nm layer of oxide is present to act as an etch stop for the xenon difluoride vapors. That protective layer is needed because tungsten is easily etched away by xenon difluoride.

Until the third mask step, all the fabrication steps remain the same using the xenon difluoride release design. At the third mask step, ammonium chloride is used to etch away the 500 nm of ZnO, and RIE is used to etch away the bottom tungsten electrode. Unique to the second design process, the 100 nm layer of silicon dioxide also needs to be removed to expose the substrate silicon layer that will be isotropically etched away by the xenon difluoride. After the silicon layer is exposed in the desired locations, a fourth mask of photoresist must be applied. The purpose of this fourth mask is to protect the inadvertent tungsten etch caused by the xenon difluoride vapors. The fourth mask creates a barrier along the sidewalls of the resonators to protect the exposed tungsten. The ZnO resonators built on silicon substrates are then released using the xenon difluoride etcher.

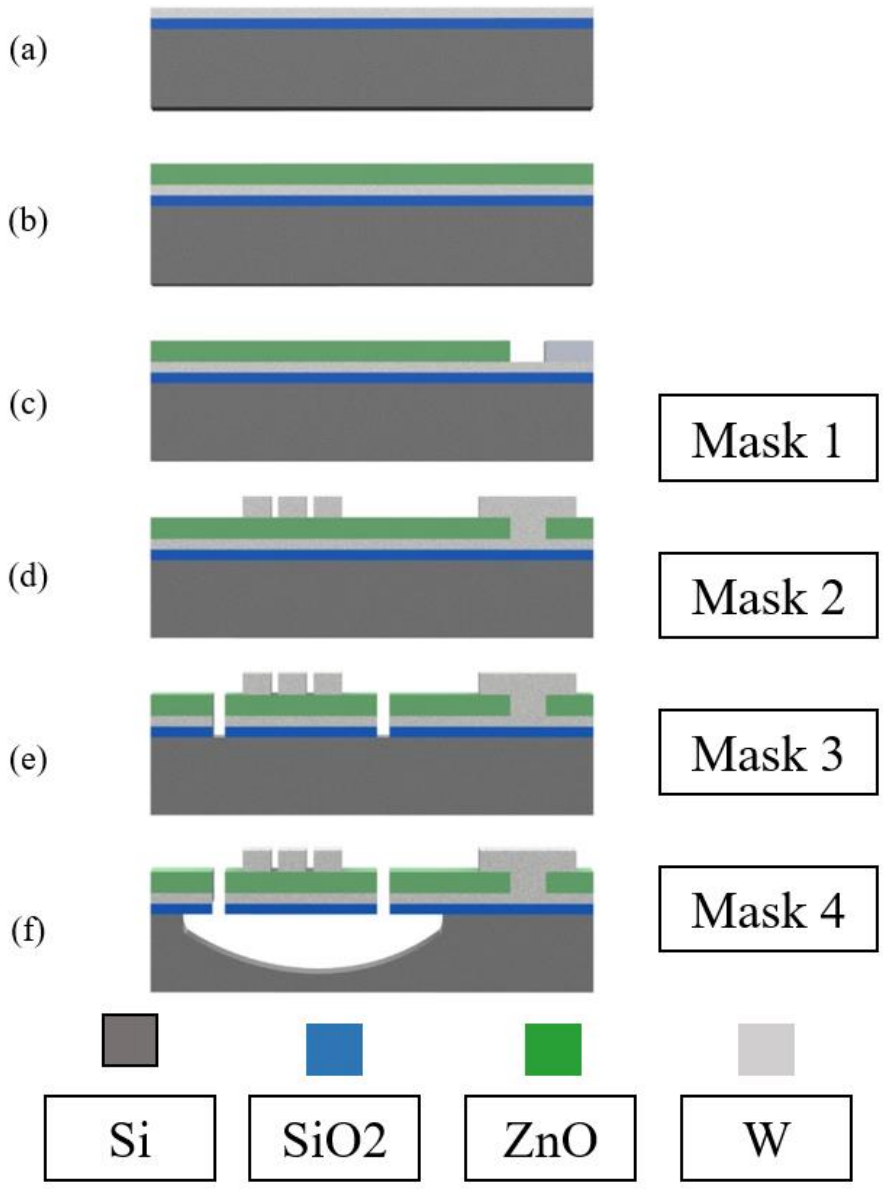

Figure 23: Fabrication process steps of piezoelectric ZnO resonators built on silicon wafers. (a) 100 nm of silicon dioxide growth and 100 nm of bottom electrode tungsten deposition. (b) 500 nm ZnO deposition. (c) Mask 1 patterning of ZnO. (d) Deposition and patterning of top electrode tungsten with mask 2. (e) Mask 3 patterning of resonator body, etching of bottom electrode tungsten, etching 100 nm layer of silicon dioxide. (f) Applying a sidewall protective photoresist layer with mask 4 and isotropic release of ZnO resonators using xenon difluoride.

3.2.6 Fully Fabricated Zinc Oxide Resonators and Filters

Figure 24 is an SEM image of the final HF released ZnO filters. Figure 25 is an SEM image of the final xenon difluoride release ZnO filter, and Figure 26 is an optical microscope image of a xenon difluoride released ZnO resonator. The results of these released resonators will be discussed in chapter 4.

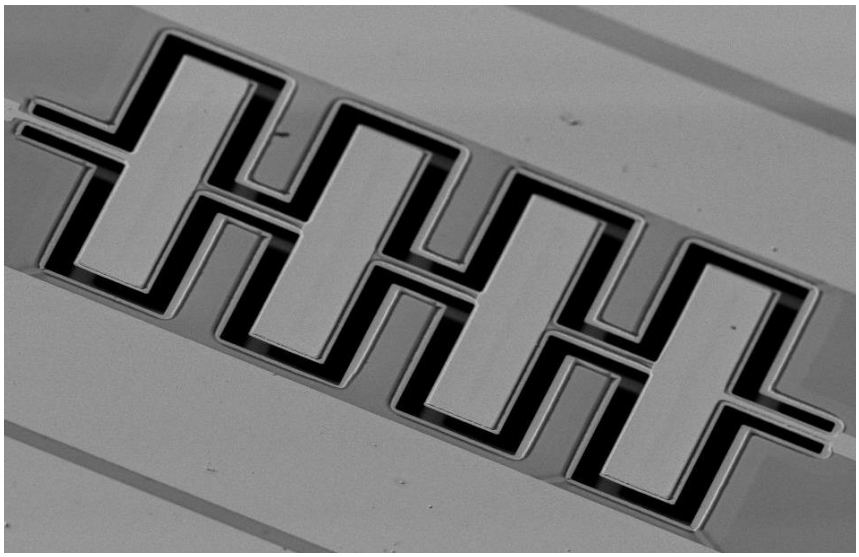

(a)

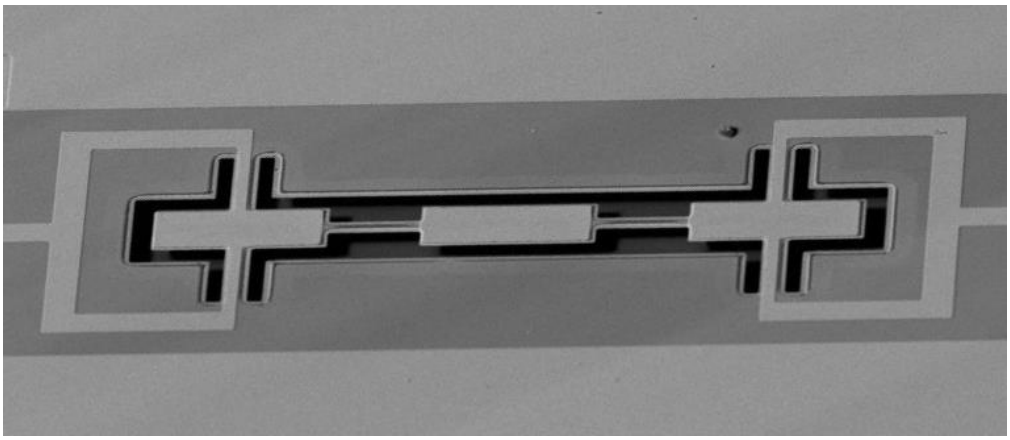

(b)

Figure 24: SEM images of fully fabricated ZnO resonators and filters released using vapor HF

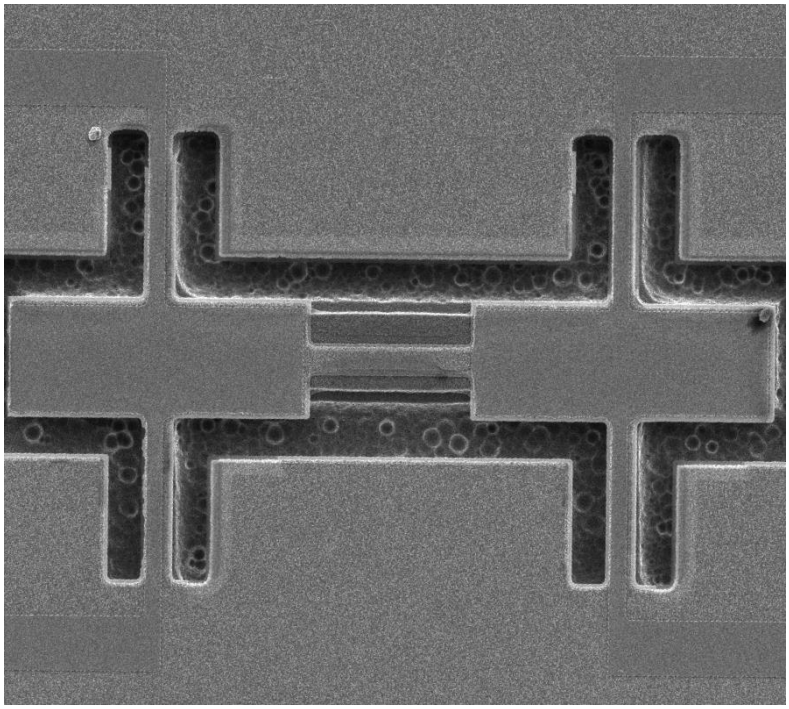

Figure 25: SEM images of fully fabricated ZnO filter released using xenon difluoride

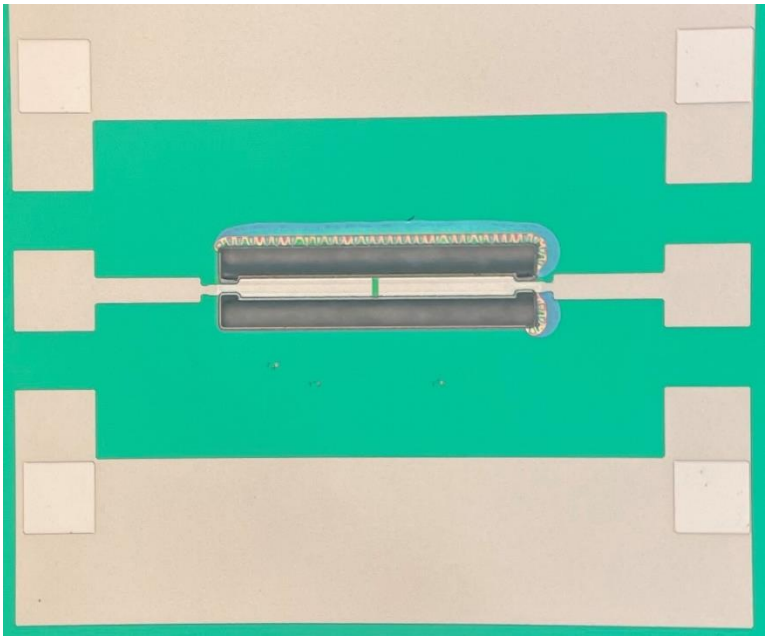

Figure 26: Optical microscope image of fully fabricated ZnO width extensional mode resonator released using xenon difluoride

3.3 Fabrication Process of Barium Strontium Titanate Resonators

The BST resonators and filters fabricated in this thesis are built similarly to the ZnO devices, so the same masks are used in the fabrication process. The main factors that distinguish BST resonator fabrication from ZnO resonator fabrication are the materials used in the design and the methods utilized to process those materials. Figure 27 shows the software layout design for the BST resonators. The metal used for the BST resonators is platinum due to its compatibility with BST and high melting point. The fabrication process flow for the BST resonators and filters can be seen in Figure 28. The next few sections in the chapter highlight the exact steps taken to process the materials for fabrication of the BST resonators and filters.

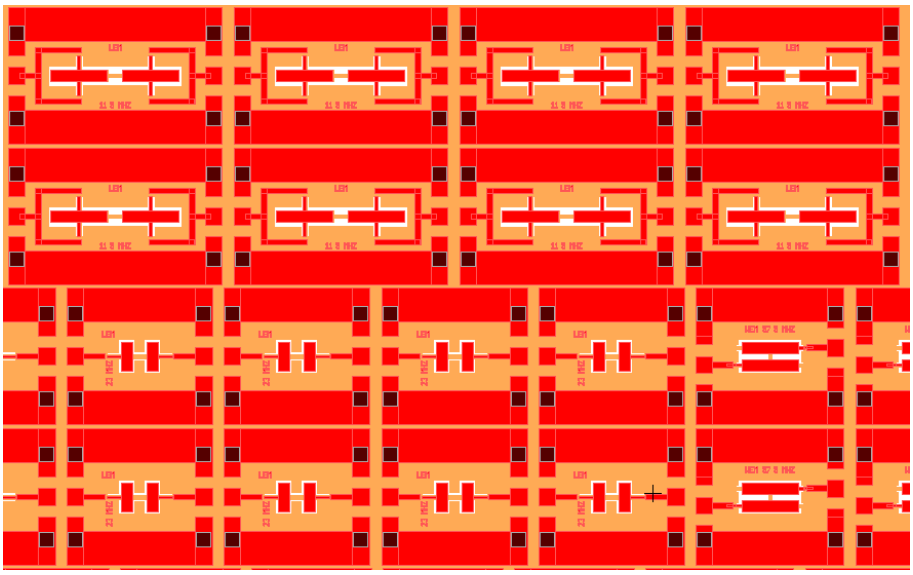

Figure 27: Layout editing software for the design of BST resonators and filters

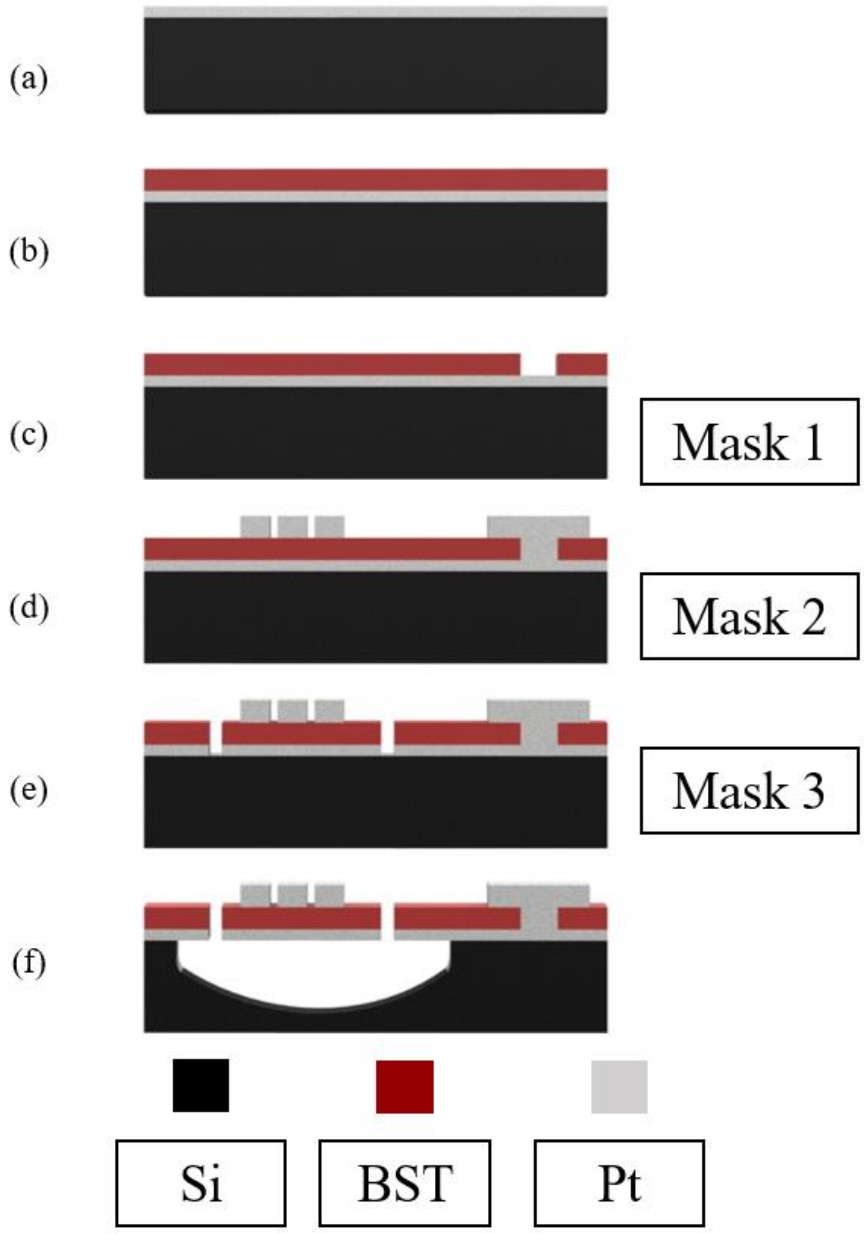

Figure 28: Fabrication process steps of piezoelectric BST resonators built on silicon wafers. (a) 100 nm of bottom electrode platinum deposition. (b) 500 nm BST deposition. (c) Mask 1 patterning of BST. (d) Deposition and patterning of top electrode platinum with mask 2. (e) Mask 3 patterning of resonator body and etching of bottom electrode. (f) Isotropic release of ZnO resonators using xenon difluoride.

3.3.1 Etching Barium Strontium Titanate Thin Film

The first fabrication step is the deposition of 100 nm of platinum on a silicon substrate. Then 500 nm of BST is deposited on top of the platinum. The first major processing step requires the selective etching of the BST layer. Mask one is used to etch the BST layer to expose small openings to the bottom platinum layer. Dry etching the BST layer using a reactive ion etching process was the first examined method. The known BST reactive ion etch recipes tend to damage the BST and prove to have slow etch rates. Additionally, BST can be wet etched using a buffered HF solution.[20] The buffered HF solution exhibits desirable characteristics and is relatively easy to use. The parameters for the buffered HF solution can be seen in Table 9.

Table 9: Buffered HF Wet Etch Parameters

Parameter	**Value**
Dilution Ratio	1:7
Temperature	Room Temp
Etch Rate	25 nm/min

3.3.2 Platinum Sputter Deposition

After the BST has been selectively etched, the top electrode, platinum, is deposited using the Kurt J Lesker Lab 18 Deposition Sputtering system. The recipe included with the sputtering system is used to deposit 100 nm of platinum. The parameters of the platinum deposition can be seen in Table 10.

Table 10: Platinum Sputter Deposition Characteristics

Parameter	Value
Ignition pressure	10 mTorr
Rotation speed	5 rpm
Power	100 W
Burn in	10 sec
Run pressure	8 mTorr
Deposition time	1200 sec

3.3.3 Reactive Ion Etching of Platinum Electrode

After the deposition of platinum, the second mask lithography step is used to pattern the top electrode. Platinum is etched using reactive ion etching, and the recipe used can be seen in Table 11. Boron trichloride and argon are used to etch away 100 nm of platinum.

Table 11: Platinum Etch Recipe

BCl_3 Flow Rate (sccm)	**Ar Flow Rate (sccm)**	**Pressure (mTorr)**	**ICP (Watts)**	**RIE (Watts)**	**Time (s)**	**Average etch rate (nm/min)**
45	5	10	800	200	600	10

3.3.4 Xenon Difluoride Etch Release for Barium Strontium Titanate Resonators

The final mask lithography is used to define the body of the resonator and filters and to expose the silicon substrate underneath. In this step, the BST is etched using a 1:7 buffered HF solution, and the bottom platinum electrode is etched using RIE. The last fabrication step is releasing the resonators and filters using a XeF_2 etcher. The parameters utilized for the XeF_2 can be seen in Table 12.

Table 12: Xenon Difluoride Etch Release Recipe

Parameter	**Value**
XeF_2 Pressure	3Torr
N_2 Pressure	2Torr
Cycle Time	60 sec
No. of Cycles	20

3.4 Simulation of Resonators

The resonators and filters designed in this thesis operate at lithographically defined frequencies. In an ideal case scenario, the resonators would operate at the defined frequencies; however, that is not always true for fabricated devices. The defined operating frequencies of the resonators can be simulated using finite element analysis tools and through mathematical equations using RLC values for electrical equivalent circuits as defined in chapter 2.

The WEM resonators in this thesis are designed to operate at 57.5 MHz. Equation 8 in chapter 2 identifies the required width of the ZnO resonator to operate at 57.5 MHz. Once the dimensions of the resonator have been defined, equations 11-13 can be used to calculate the RLC values for the electrical equivalent circuit modeling. The values of R_m, C_m, and L_m are 18 Ω, 31 fF, and 217 μH, respectively. These values can be plugged into a circuit simulation software that exhibits electrical resonance near 57.5 MHz. Figure 29 illustrates the simulated electrical resonance of the WEM resonator. The series resonance occurs when the impedance is at its minimum or when the inductive reactance is equal and opposite of the capacitive reactance.

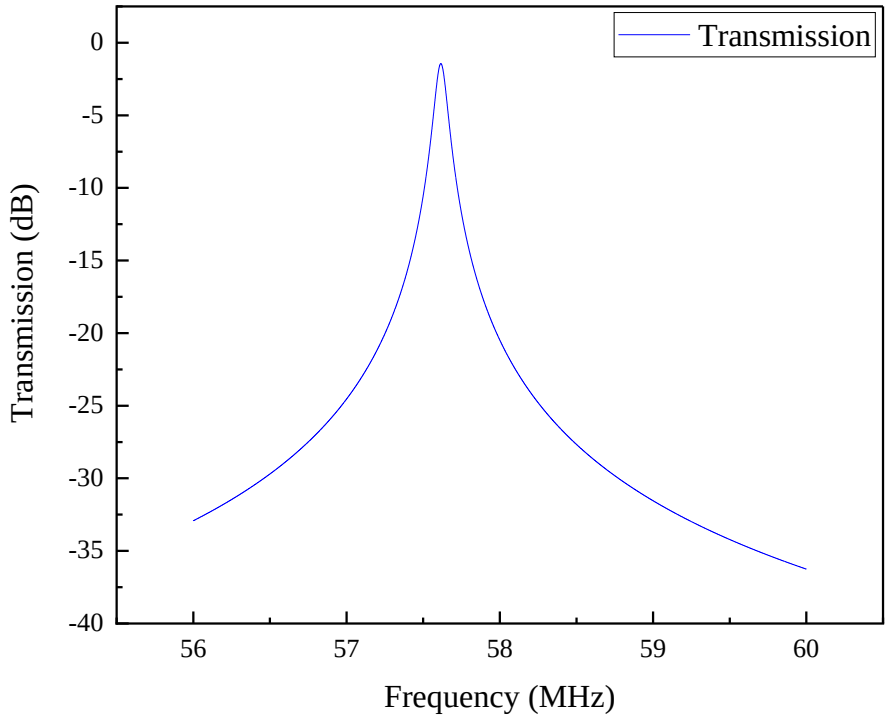

(a)

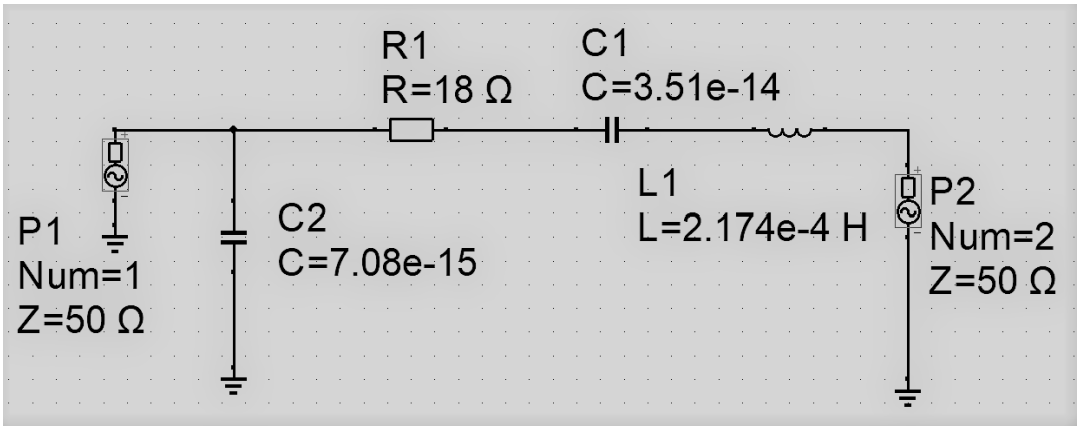

(b)

Figure 29: (a) Simulated electrical response of width extensional mode resonator at 57.5 MHz based on (b) equivalent RLC circuit Butterworth Van Dyke Model

3.5 Experimental Fabrication Methods

In the fabrication of the MEMS resonators and filters found in this thesis, many different techniques were investigated. The ultimate goal was to develop methods to process the unique materials required to build the resonators and filters. In pursuit of that goal, many of the techniques attempted led to undesirable results. The purpose of this section is to highlight the unsuccessful attempts to prevent repetition of the same mistakes in future work.

3.5.1 Aluminum as Resonator Electrode

The final design of the ZnO resonators was completed using tungsten as the electrode; however, aluminum was initially the metal chosen for electrodes. Aluminum has a high melting temperature, a desirable characteristic, and can be easily deposited in the AFIT cleanroom. The issue with using aluminum in the process is that the top electrode needs to be patterned according to the design requirements. Patterning the top electrode means selectively etching the aluminum using reactive ion etching or a wet etch solution. The solution required to wet etch aluminum can unintentionally react with other materials in the design. In order to avoid unintended consequences, a dry etch approach seemed best. However, AFIT's cleanroom does not possess chlorine and argon in the reactive ion etcher. For this reason, aluminum was exchanged for tungsten.

3.5.2 Reactive Ion Etching of Zinc Oxide

As stated in section 3.2, the most efficient method of etching ZnO was using an ammonium chloride wet etch solution. However, the initial technique used to etch ZnO was through a reactive ion etcher. The parameters for the recipe can be seen in table 13

Table 13: ZnO RIE Recipe

Cl_2 Flow Rate (sccm)	**Ar Flow Rate (sccm)**	**Pressure (mTorr)**	**ICP (Watts)**	**RIE (Watts)**
20	5	5	300	35

The results from this experiment proved to be unsuccessful. The RIE recipe etched the ZnO layer very slowly and mainly attacked the protective S1818 photoresist layer. Secondly, the gases need for this RIE recipe are not available in the AFIT cleanroom, so this etch process had to be conducted at AFRL. For those stated reasons, wet etching ZnO thin films with ammonium chloride was determined to be the most efficient approach.

3.5.3 Tungsten Electrode Protection Methods

The original ZnO resonators and filters were designed to be fabricated on silicon wafers as opposed to final design of silicon dioxide wafers. The major difference in using silicon wafers versus silicon dioxide wafers is the vapor used to release the resonators. Silicon wafers are isotropically etched in presence of xenon difluoride, and silicon dioxide wafers are isotropically etched by hydrogen fluoride vapors.

Following the original design, the ZnO resonators were built on silicon wafers with tungsten as the choice for the top and bottom electrodes. The final fabrication step is releasing the ZnO resonators using a xenon difluoride vapor. After the etch, it was discovered that the xenon difluoride not only etches way the silicon substrate but also the tungsten electrodes. Figure 30 below shows that the electrode beams are properly intact before the etch cycle. Figure 31 highlights the discontinuity of the input electrode to the rectangular resonator body.

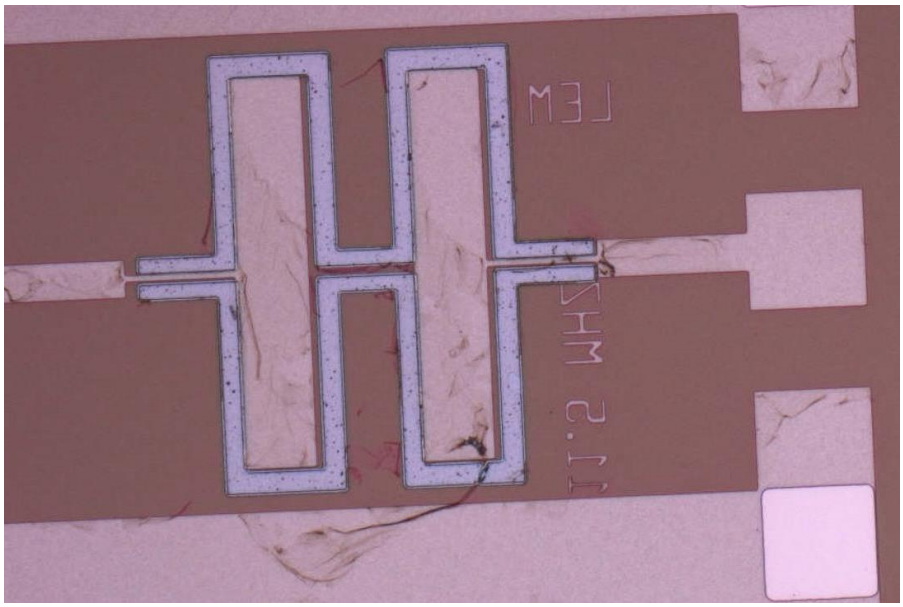

Figure 30: ZnO filters before placement in the XeF_2 etcher. The tungsten tethers connecting to the input and output of the resonators are still intact

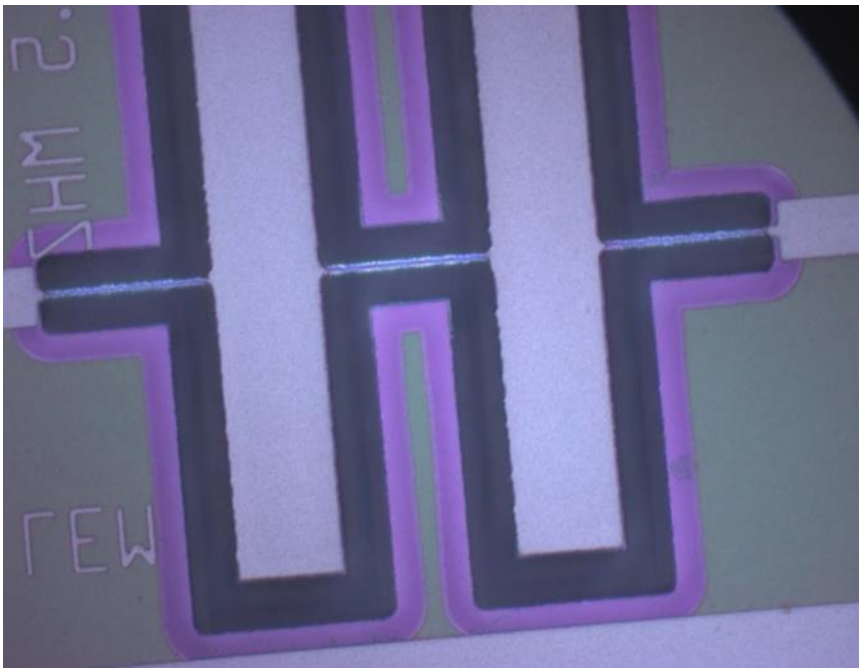

Figure 31: ZnO filters after placement in the XeF_2 etcher. The tungsten tethers connecting to the input and output of the resonators have been completely etched away by XeF_2

The results from this test prompted the exploration of multiple strategies to protect the tungsten layer while conducting a xenon difluoride release process.

3.5.3.1 Building Larger Tethers

The first attempt to protect the tungsten from xenon difluoride consisted of double the size of the tungsten lines connecting to the resonators. This method proved to be insufficient because the top electrode was still being completely etched away. Secondarily, the bottom electrode remains unprotected and will be etched away by the xenon difluoride vapor.

3.5.3.2 Building an Etch Stop

The second method used to protect the tungsten electrode was building an etch stop layer made of silicon dioxide. Silicon dioxide is not affected by xenon difluoride. In this protection method, the top electrode tungsten is protected by photoresist, and the bottom electrode is protected by silicon dioxide. The 100 nm silicon dioxide etch stop layer was grown in the oxidation furnace at AFIT. Before the growth of the oxide, the silicon wafers were thoroughly cleaned using a RCA clean to remove any contaminants. Unfortunately, this protection did not prove to be successful. As shown in Figure 32, the silicon dioxide etch stop layer only partially worked. The photoresist and silicon dioxide layers protected the tungsten from the top and bottom, but the sidewalls are still exposed. The exposed sidewalls allowed the xenon difluoride to slowly etch away the tungsten. The shape of the electrodes should be perfect rectangles, but the sidewall attack by the xenon difluoride caused jagged edges after a short cycle in the vapor. This discovery prompted the employment of a mask 4 photoresist layer to protect the sidewalls during a xenon difluoride release as stated in section 3.2.5.

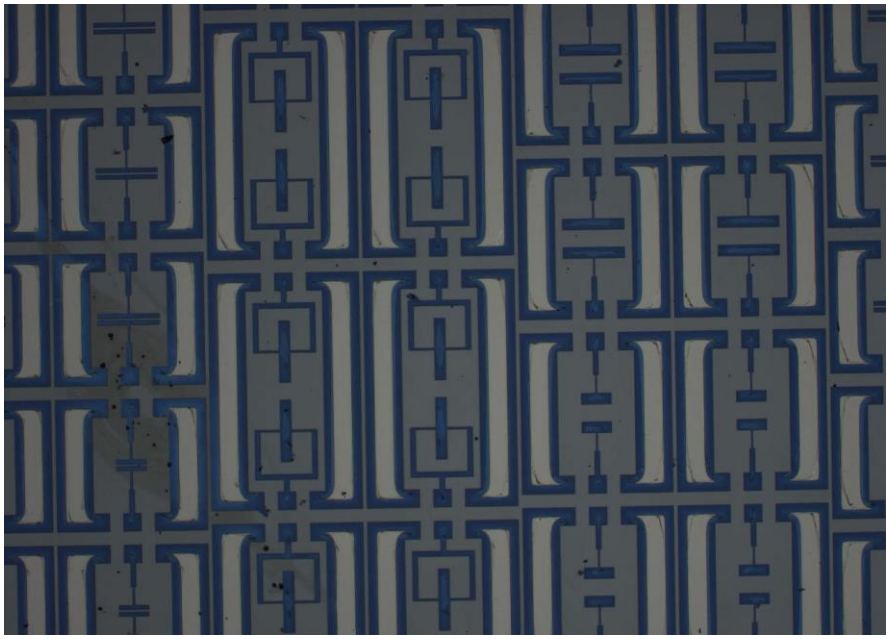

(a)

(b)

Figure 32: Bottom etch stop layer of silicon dioxide alone is not sufficient enough to protect the tungsten electrodes during a XeF_2 etch. The XeF_2 vapors still attack the tungsten from the sidewalls and cause the jagged edges along electrode body

3.5.4 Characterizing Oxygen Plasma Asher

Common to every cleanroom is a plasma asher. An oxygen plasma asher is an excellent tool to remove photoresist from a sample after processing. The equipment operates by creating a vacuum environment to ionize the oxygen gas into a plasma. The reactive plasma combines with the photoresist layer to form a byproduct that is removed using a vacuum pump.

The standard method of removing photoresist entails a solvent clean using acetone, methanol, and isopropyl. In the context of this thesis, that cleaning strategy is not viable because the sample must be spinning on a chuck and sprayed with the solvents. The final freestanding resonators and filters will breakaway using the standard cleaning methods. For this reason, the plasma asher was employed to remove the photoresist.

The thickness of S1818 photoresist used in this thesis is approximately 1.8 to 2 microns. After a careful etch study, it was determined that the AFIT plasma asher has etch rate of roughly 12 nm/min for S1818 photoresist. In order to remove upwards of 2 microns of photoresist, the sample must be placed in the plasma asher for 170 minutes. The reason for the incredibly slow etch rate is because AFIT's plasma asher is not temperature controlled. Increasing the temperature during ashing will significantly decrease the processing time. As a result of this limitation, the photoresist was removed using a reactive ion etcher. The reactive ion etcher only requires 3 minutes to remove 2 microns of photoresist. The potential downside to using a reactive ion etcher is that the physical bombardment of ions can damage a sample; however, there was no indication of that disadvantage in this thesis.

3.5.4 Reactive Ion Etching Recipe to Etch Platinum

In the design of the BST resonators, the electrodes used to excite the BST layer are made up of platinum. These electrodes must be carefully patterned to meet the design requirements. Platinum can be patterned using a wet solution or with a dry reactive ion etcher. The most commonly used wet etch solution for platinum is a mixture of nitric acid and hydrochloric acid known as aqua regia.[45] This solution was not used in this thesis due to concerns over the effects of the aqua regia solution on the other materials used in the design of the BST resonators.

The alternative approach to etch platinum is using mixture of chlorine and argon gas in a reactive ion etcher. The reactive ion etcher provides anisotropic etch profile that produces extremely consistent results. The difficulty with reactive ion etching is determining the correct parameters to conduct the etch and choosing the correct protective layer to etch only the defined areas of platinum. The typical protective layer in an etching process is photoresist. The three photoresists used to protect platinum during the RIE process were S1818, SPR-220, and S1827. SPR-220 and S1827 were difficult photoresists to expose and develop because those are not commonly used photoresists in the AFIT cleanroom. S1818 served as the masking layer for the initial RIE of platinum tests. During these initial tests, the chamber pressure and power settings of the etch process were set at low values. This resulted in extremely low etch rates of the platinum and high etch rates for the protective photoresist layer. The parameters for the unsuccessful platinum etch can be seen in Table 14.

Table 14: Unsuccessful Platinum RIE Recipe

Cl_2 Flow Rate (sccm)	**Ar Flow Rate (sccm)**	**Pressure (mTorr)**	**ICP (Watts)**	**RIE (Watts)**
20	5	5	300	35

The correct recipe can be seen in section 3.3.3. The difference in the successful recipe is the increased flow rate of the gases and the higher inductively coupled plasma power setting.

IV. Analysis and Results

4.1 Chapter Overview

This chapter discusses the measurement results of the fabricated resonators and filters. The fabricated resonators were measured using a vectored network analyzer after a careful short, open, load, and trough (SOLT) calibration of the system. A vectored network analyzer uses S-parameters to measure the transmission and reflection response of two port devices, such as the resonators built in this thesis. S-parameters provide unique quantification of how RF energies propagate through a two port system. S-parameters are elements of the scattering matrix that give ratio of the reflected signal to the transmitted signal at each port.

4.2 Results of Zinc Oxide Resonators

The ZnO resonators were characterized with a network analyzer in ambient air. The results show that there was no resonance detected at the designed frequency. Figure 33 shows the measured transmission of the 57.5 MHz WEM resonators. As the figure shows, there is no resonance detected and the noise floor of the resonator is higher than expected. A few different resonators and filters cross the chip were characterized using the network analyzer. There was no resonance detected from any of the ZnO devices. The transmission responses from additional ZnO devices can be seen in appendix A.

The lack of a proper response from the released ZnO resonators prompted additional analysis to understand the root cause of the issue. The fabrication of the resonators did not exhibit any design flaws, and the resistance seen in the tungsten

electrodes was relatively low. This only left the quality of the ZnO as the unknown in the design.

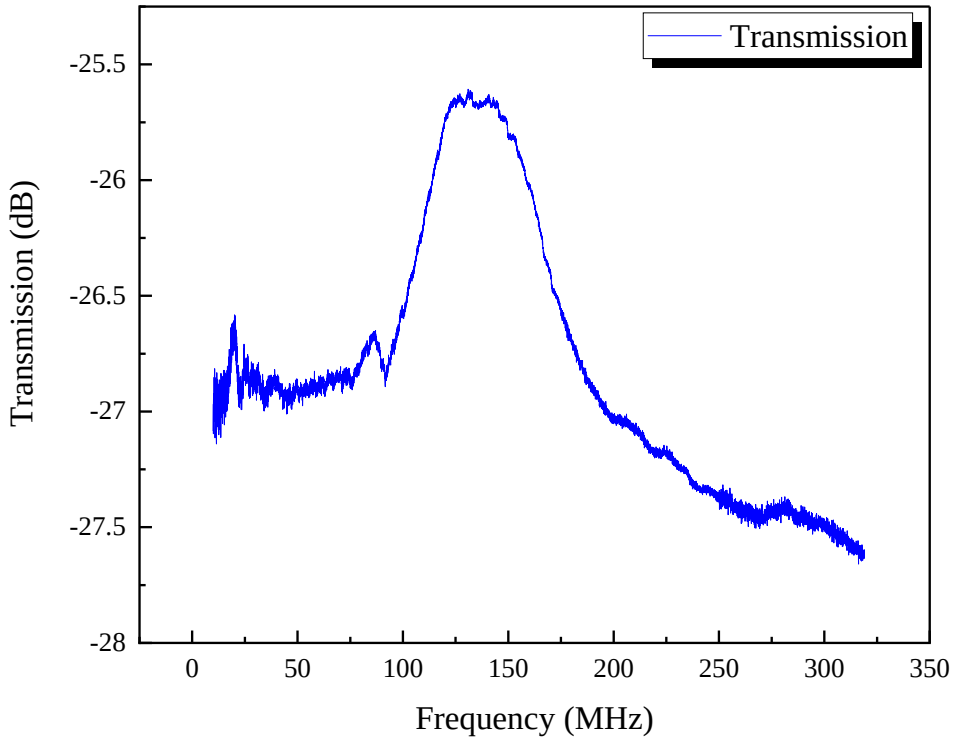

Figure 33: Measured frequency response from a 57.5 MHz ZnO width extensional mode resonator built on a silicon dioxide wafer. Frequency response is mostly noise and no mechanical resonance is detected

4.2.1 Zinc Oxide Thin Film Analysis

The first method used to test the piezoelectric properties of the ZnO was based on the piezoelectric effect. Under applied mechanical stress, ZnO thin films should produce a small voltage equal to its piezoelectric coefficient of 4 pm/V.[46] However, there was no voltage observed on the oscilloscope in the WEM resonators when a force was applied using a microprobe.

X-ray diffraction (XRD) characterization was the second method utilized to analyze the ZnO film. XRD is an excellent characterization tool that identifies the structural properties of thin films. ZnO exhibits the maximum levels of piezoelectricity when the film is grown in the c-axis orientation. A ZnO thin film with high c-axis orientation will show an intensity peak around 34° for the 002 crystal orientation. Figure 34 shows the XRD data of the ZnO grown on tungsten on a silicon dioxide layer used to build the resonators in this thesis. The ZnO used in thesis does not exhibit the correct growth orientation which explains why there was no resonance detected at the designed frequencies. The sharp intensity peak near 70° is indicative of the (201) plane which suggests a crystalline defect in the ZnO thin film.[47]

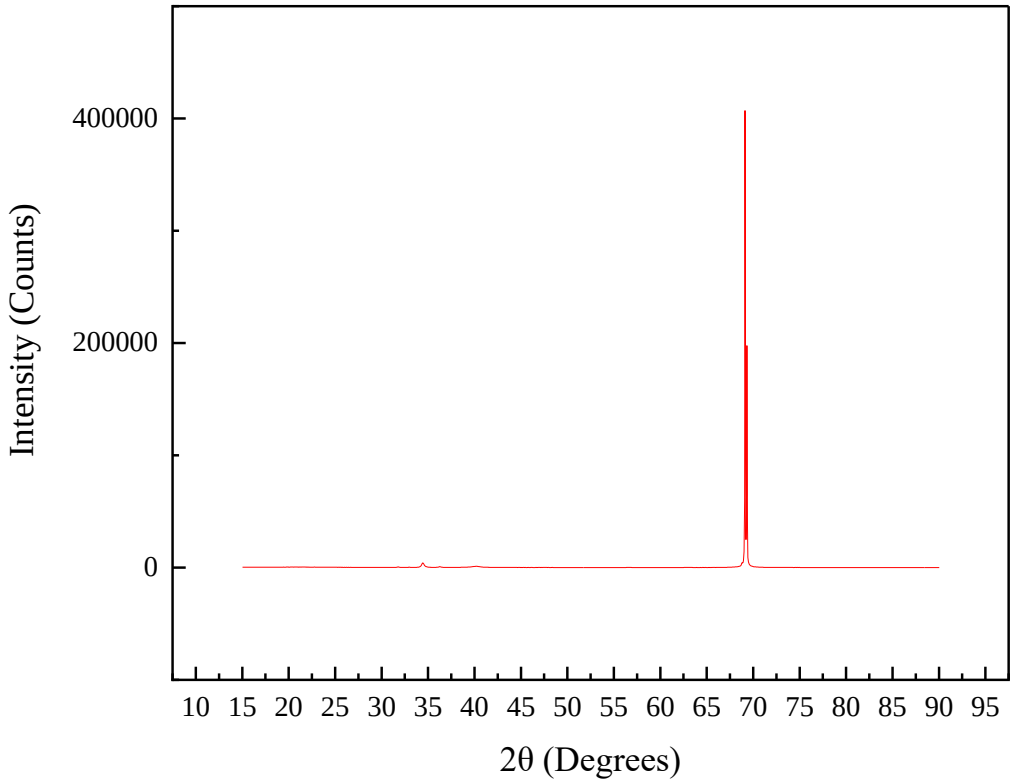

Figure 34: XRD data measured from ZnO sample deposited on tungsten on a SiO_2 wafer

In addition to the XRD data, SEM images of the ZnO thin film surface show large grain boundaries as shown in Figure 35. These large grain boundaries can be indicative of poor film quality which leads to suppressed piezoelectric properties from the ZnO.

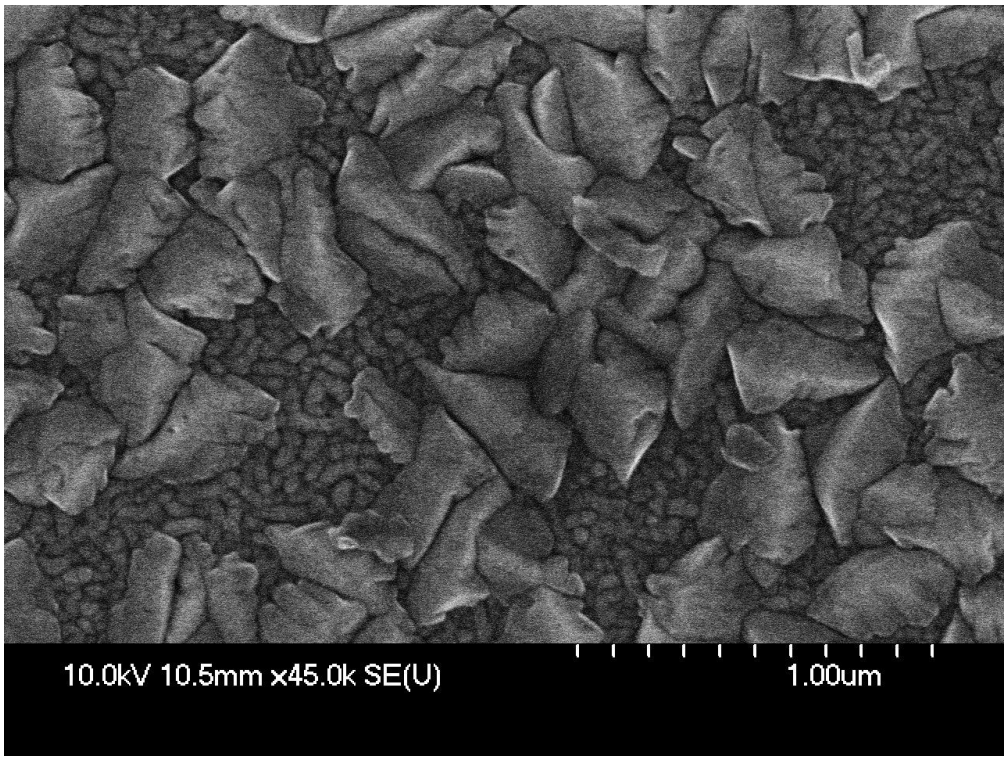

Figure 35: SEM of surface of ZnO grown on tungsten. SEM shows large unwanted grain boundaries.

4.3 Results of Barium Strontium Titanate Resonators

The fabricated BST resonators did not produce desirable results. After the final release step, all the resonators broke at the tethers under stress. Figure 36 is an optical microscope image of the BST resonators following the xenon difluoride etch release step. The image shows the cracks forming in the film which caused the resonator tethers to snap.

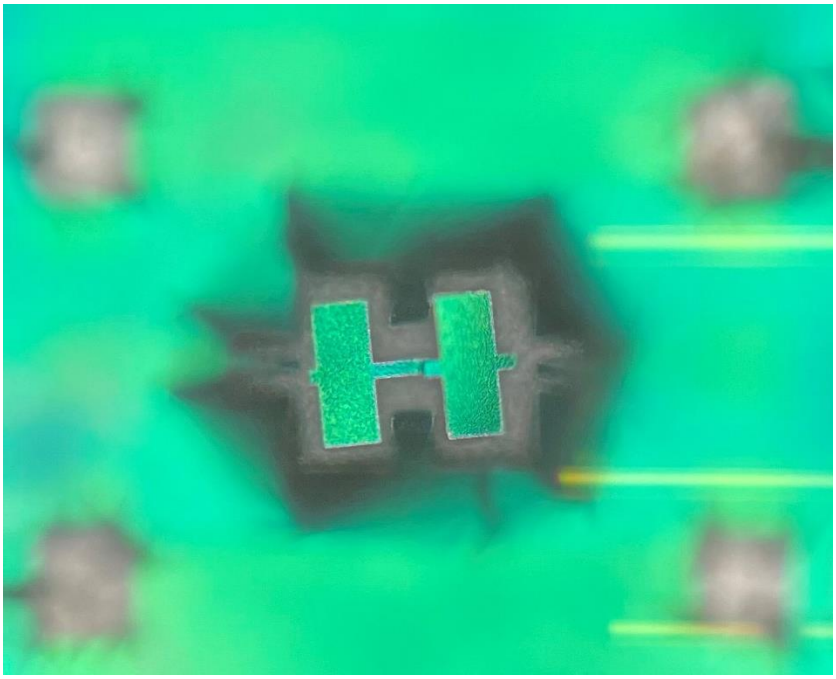

Figure 36: Fully released BST resonators using XeF_2. The BST film began to crack and the resonators broke at the anchor points

4.4 Surface Acoustic Wave Resonators

In order to identify the poor film quality as the main concern for poor response of the released resonators, surface acoustic wave (SAW) resonators were built to test the piezoelectricity of the ZnO and BST thin films. SAW resonators are relatively simple devices to build because they require only one photolithography mask. SAW resonators operate on piezoelectric materials with the help of interdigitated transducers that convert electrical signals into acoustic waves and vice versa. The frequency of operation of SAW resonators can vary based on many factors, but the main design parameter is the pitch of the interdigitated fingers.

4.4.1 Zinc Oxide Surface Acoustic Wave Resonators

The SAW devices were built on the chips with ZnO deposited on a silicon wafer. Figure 37 shows the results of the ZnO SAW resonator. The SAW devices are designed for resonance around 150 MHz, so the transmission drop around 25 MHz is large due to the parasitic capacitance between the interdigitated transducers.

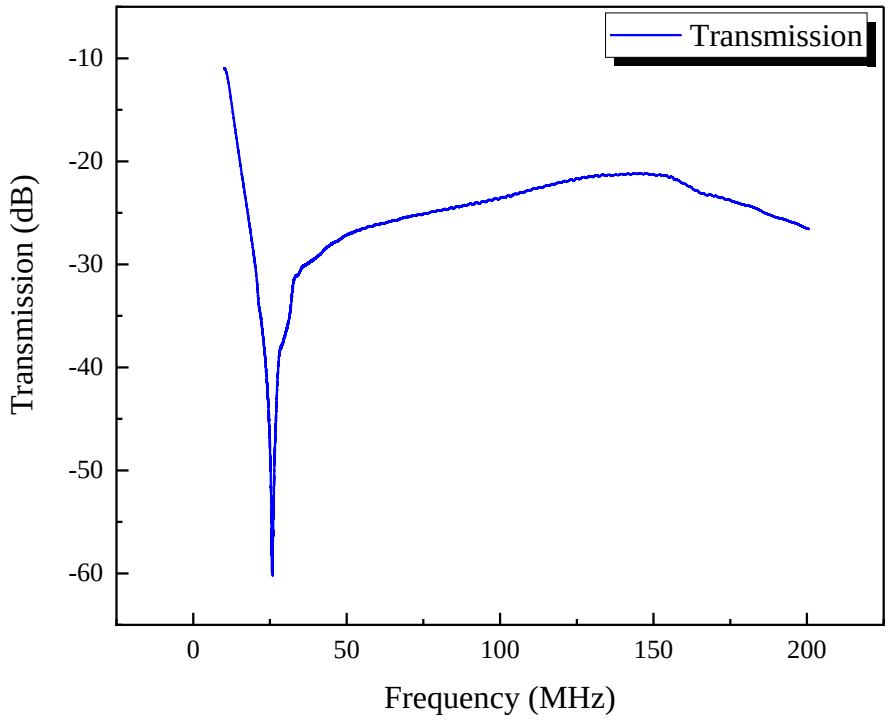

Figure 37: Measured frequency response from a ZnO SAW resonators. The designed frequency is near 150 MHz. The sharp drop in transmission at 25 MHz is due to the parasitic capacitance of the interdigitated transducers of the SAW device.

4.4.2 Barium Strontium Titanate Surface Acoustic Wave Resonators

The BST SAW resonators required a DC bias of 15V for device operation. However, there was no mechanical resonance detected for the BST SAW resonators as

shown in Figure 38. Again, the sharp dip in transmission near 15 MHz could be due to parasitic capacitance. Characterization beyond 50 MHz only returned results of noise.

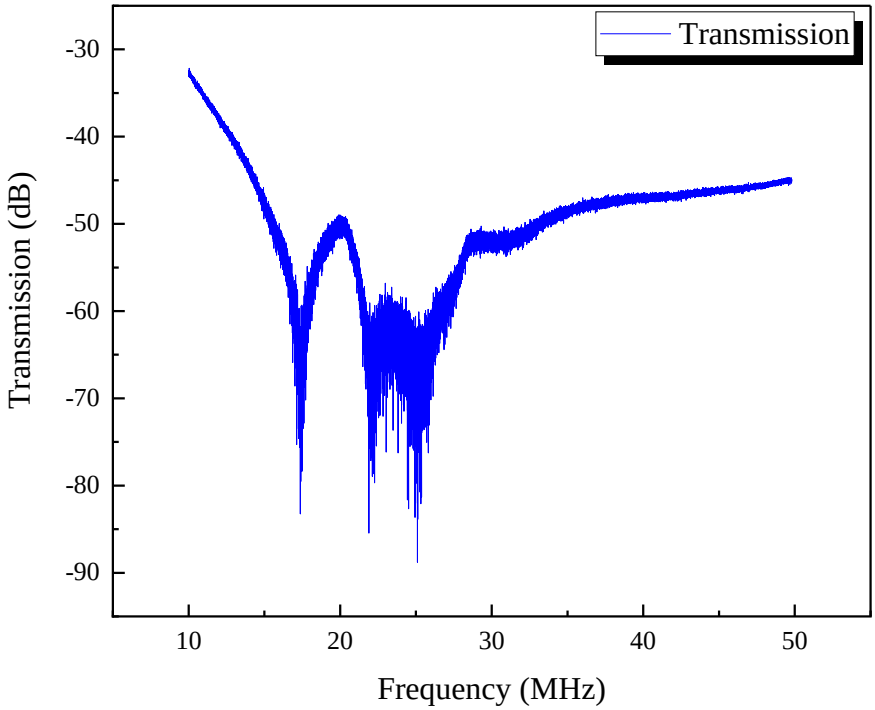

Figure 38: Measured frequency response from a BST SAW resonators. The designed frequency is near 150 MHz. There is no mechanical resonance detected in the BST SAW resonator.

4.4.3 Scandium Aluminum Nitride Surface Acoustic Wave Resonators

In order to verify the design of the SAW resonators, a commercially deposited thin film of scandium doped aluminum nitride (ScAlN) was used to illustrate proper resonance. The ScAlN piezoelectric thin film has been vetted and has the optimum growth orientation for maximum piezoelectricity. Figure 39 shows the measured transmission response of the SAW resonator built on ScAlN. The ScAlN SAW resonators demonstrates a proper resonance and anti-resonance peak near the designed 150 MHz.

The working ScAlN SAW resonator helps validate the resonator designs and isolates the ZnO and BST thin films as main factors in the lack of resonance.

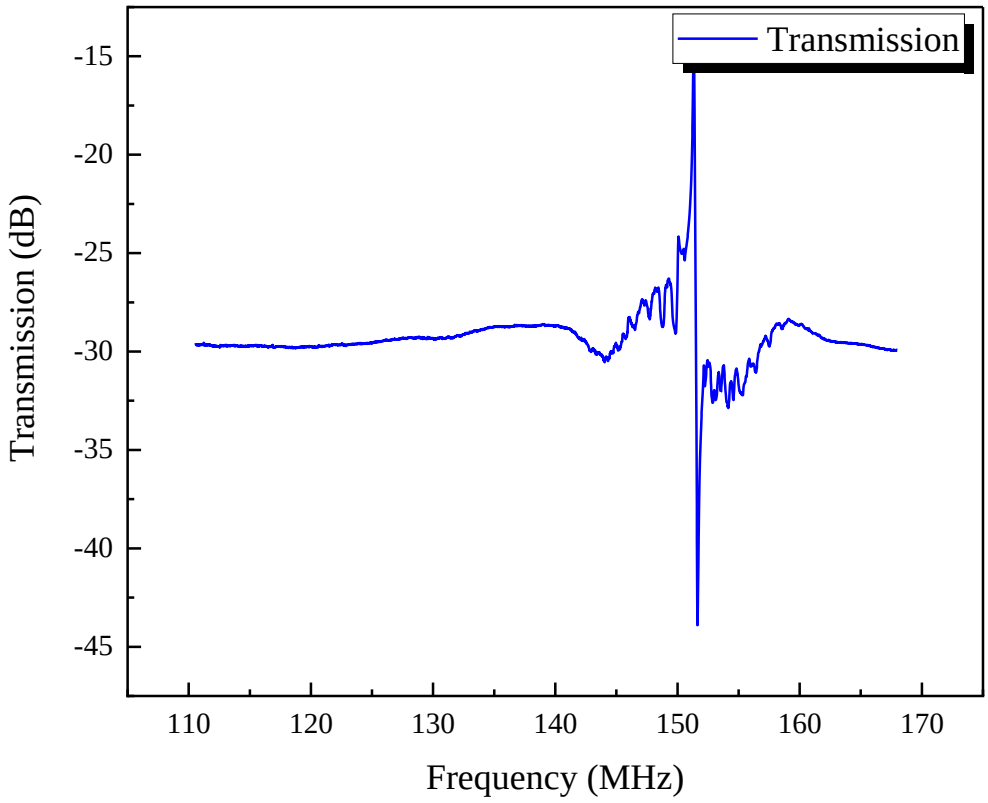

Figure 39: Measured frequency response from a ScAlN SAW resonators. The designed frequency is near 150 MHz. This SAW resonator exhibits a strong mechanical resonance with sharp resonance peak and sharp anti-resonance dip

4.5 ScAlN Filter Response

The transmission response from the ScAlN SAW device is only of one resonator. However, that resonator can be coupled in a simulation or with inductors and capacitors

to exhibit the response of a working filter.[48] Figure 40 illustrates the various filter topologies that can be implemented using a singular resonator.

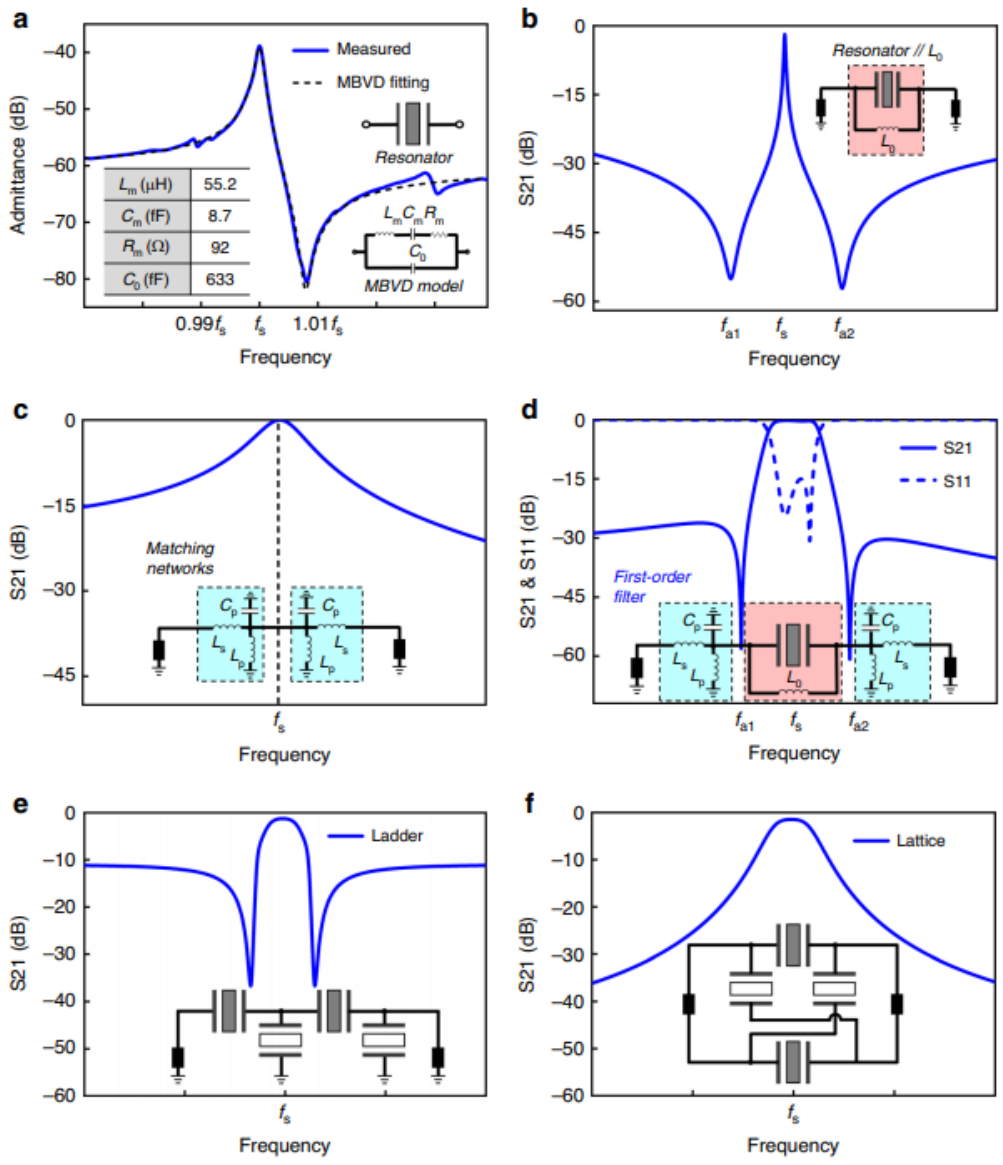

Figure 40: Topology and principles of first-order ScAlN filters. Single resonators can be lumped with inductors and capacitors to form a bandpass filter response with the help of a matching network [48]

With combination of capacitors and inductors in a matching network configuration, a robust bandpass filter response can be generated near the center frequency of the singular resonator.

V. Conclusions and Recommendations

5.1 Chapter Overview

This chapter provides conclusion from the results of the thesis work. In this chapter, the significance of the research is discussed along with the recommendations for future work.

5.2 Conclusions of Research

Fabrication of thin film piezoelectric resonators and filters is an incredibly meticulous undertaking. Successful handling of the delicate material used in the designs is key to producing operational devices. Unfortunately, the quality of the ZnO and BST thin films limited the research scope of this thesis. However, significant milestones were achieved in the process, and the knowledge base of the AFIT Cleanroom was vastly expanded.

5.3 Significance of Research

Through this master's thesis, an innovative concept of building contour mode resonators was discovered. Conventionally, resonators with tungsten electrodes cannot be released using xenon difluoride because tungsten is rapidly etched by xenon difluoride. In this thesis, a method using photoresist as a sidewall protection layer during the xenon difluoride etch was validated. Additionally, study on statistical enhancements of etching ZnO thin films with ammonium chloride added to the research body of knowledge.

5.4 Recommendations for Future Research

Improvement of the quality of the ZnO and BST thin films is an absolute priority for future research. There are many factors that impact of the quality of thin film growth. The ZnO and BST films in this thesis were grown directly on the top electrode. Those bottom electrodes were deposited using AFIT's sputtering system. Significant surface roughness can impact the grow orientation of the thin film and introduce large grain boundaries. The surface roughness can be reduced by implementing a thin buffer oxide layer into the resonator stack. The buffer oxide layer would be grown on top of the bottom electrode and become the base layer for ZnO or BST.[7]

In addition to the oxide layer, a comprehensive study should be conducted on the effects of annealing temperature and time on the quality of ZnO. Annealing temperature and annealing time are significant factors in the quality of ZnO thin films.[49] A two factor study, based on annealing time and temperature, should be used to optimize the ZnO deposition process. The study should use XRD data and SEM images to monitor the quality of the ZnO films.

VI. Appendix A

The ZnO design layout consisted of many resonators and filters fabricated on a single chip. Unfortunately, no mechanical resonance was detected for any of the resonators and filters due to the poor quality of the ZnO thin film. Figure x below depicts the frequency response of a length extensional mode filter.

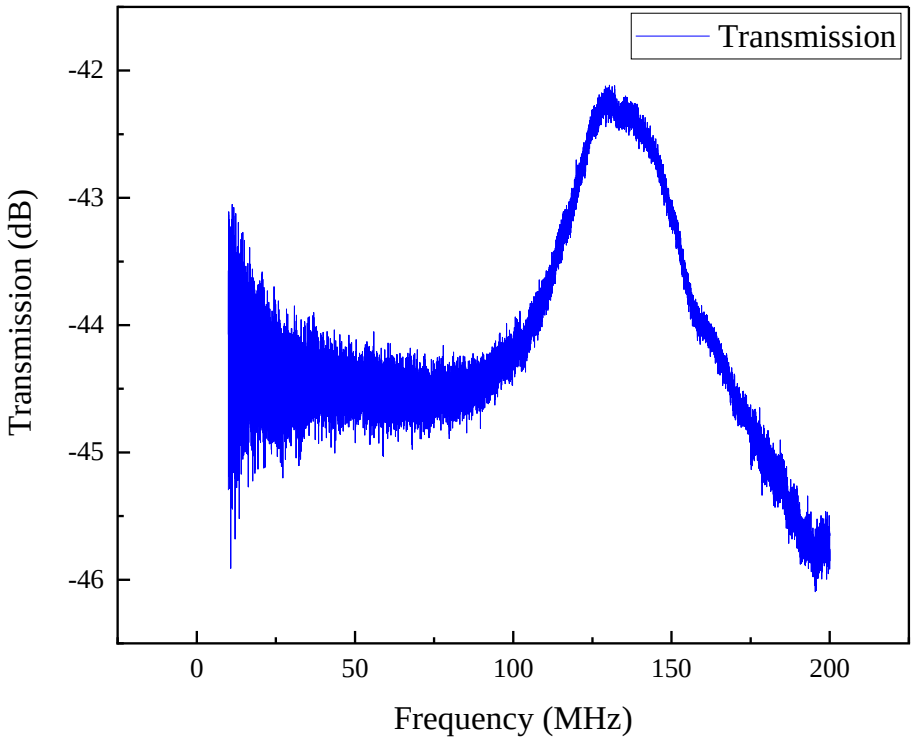

Figure 41: Measured frequency responses from a ZnO length extensional mode filter built on a silicon dioxide wafer. The noise floor of the frequency response is lower compared to the stand alone filters but still no mechanical resonance is detected.

In an attempt to enhance the response of the ZnO resonators, a 5V DC bias was applied to a width extensional mode resonator. The application of the DC bias did not provide a

better response. The DC bias only lowered the noise floor level when compared to the unbiased response.

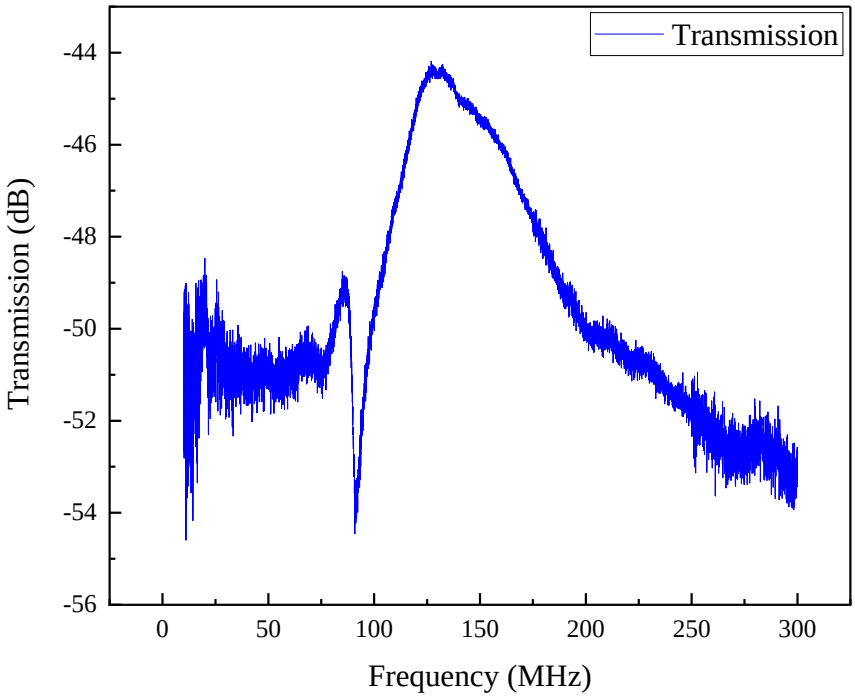

Figure 42: Measured frequency responses from a ZnO width extensional mode resonator with a 5V DC bias built on a silicon dioxide wafer. The frequency response is lower compared to the stand alone filters but still no mechanical resonance is detected.

VII. Appendix B

For the simulation of the resonators used in the thesis, values of the motional resistance, capacitance, and inductance were calculated using Matlab. The sample Matlab code for a length extensional mode resonator can be seen below.

```
clc
clear
%%LEM MHz

Ep = 110E9;
d31 = 4.7E-12;
rho = 5610;
Q = 5000;
n = 1;

L = 200E-6;
W = 40E-6;
t = 0.5E-6;

eta = 2.*Ep.* d31.* W;
eta2 = eta.^2;

Meff = rho.*L.*W.*t./2;
Keff = n.*Ep.*t.*W.*pi.*pi./(2.*L);

Rx = sqrt(Keff.*Meff)./(Q.*eta2);
Cx = eta2./Keff;
Lx = Meff./eta2;

Fo = 1./(sqrt(Lx.*Cx).*(2.*pi));

fprintf('Rx is equal to: %.3d ohms\n', Rx);
fprintf('Cx is equal to: %.3d F\n', Cx);
fprintf('Lx is equal to: %.3d Henry\n', Lx);

fprintf('Fo is equal to: %.3d Hertz\n', Fo);
```

Bibliography

[1] W. T. Hsu, “Vibrating RF MEMS for timing and frequency references,” *IEEE MTT-S Int. Microw. Symp. Dig.*, pp. 672–675, 2006, doi: 10.1109/MWSYM.2006.249704.

[2] M. Rais-Zadeh, V. A. Thakar, Z. Wu, and A. Peczalski, “Temperature compensated silicon resonators for space applications,” *Reliab. Packag. Testing, Charact. MOEMS/MEMS Nanodevices XII*, vol. 8614, no. March 2013, p. 86140E, 2013, doi: 10.1117/12.2001434.

[3] N. Korobova, V. Vodopyanov, and S. Timoshenkov, “Design and fabrication of piezoelectric MEMS,” *Int. Conf. Micro- Nano-Electronics 2012*, vol. 8700, p. 87000R, 2013, doi: 10.1117/12.2016968.

[4] P. K. Panda, “Review: Environmental friendly lead-free piezoelectric materials,” *J. Mater. Sci.*, vol. 44, no. 19, pp. 5049–5062, 2009, doi: 10.1007/s10853-009-3643-0.

[5] H. Zhu, G. C. Shan, C. H. Shek, and J. E. Y. Lee, “Shear dependent nonlinear vibration in a high quality factor single crystal silicon micromechanical resonator,” *Appl. Phys. Lett.*, vol. 101, no. 3, 2012, doi: 10.1063/1.4737213.

[6] H. M. Lavasani, W. Pan, B. Harrington, R. Abdolvand, and F. Ayazi, “A 76 dBΩ 1.7 GHz 0.18 μm CMOS tunable TIA using broadband current pre-amplifier for high frequency lateral MEMS oscillators,” *IEEE J. Solid-State Circuits*, vol. 46, no. 1, pp. 224–235, 2011, doi: 10.1109/JSSC.2010.2085890.

[7] R. Abdolvand, “THIN-FILM PIEZOELECTRIC-ON-SUBSTRATE RESONATORS AND NARROWBAND FILTERS,” Georgia Institute of Technology.

[8] R. F. Mould, “Pierre Curie, 1859-1906,” *Curr. Oncol.*, vol. 14, no. 2, pp. 74–82, 2007, doi: 10.3747/co.2007.110.

[9] A. American and N. Standard, “An American National Standard: IEEE Standard on Piezoelectricity,” *IEEE Trans. Sonics Ultrason.*, vol. 31, no. 2, pp. 8–10, 1984, doi: 10.1109/T-SU.1984.31464.

[10] G. Pillai and S.-S. Li, “Piezoelectric MEMS Resonators: A Review,” *IEEE Sens.*

J., vol. XX, no. XX, pp. 1–1, 2020, doi: 10.1109/jsen.2020.3039052.

[11] H. Bhugra and G. Piazza, *Piezoelectric MEMS Resonators*. Springer International Publishing Switzerland, 2017.

[12] Y. Yuan *et al.*, "A ZnO thin-film driven microcantilever for nanoscale actuation and sensing," *Int. J. Smart Nano Mater.*, vol. 4, no. 2, pp. 128–141, 2013, doi: 10.1080/19475411.2012.749959.

[13] S. S. Balpande, R. S. Pande, and R. M. Patrikar, "Design and low cost fabrication of green vibration energy harvester," *Sensors Actuators, A Phys.*, vol. 251, pp. 134–141, 2016, doi: 10.1016/j.sna.2016.10.012.

[14] J. Kim *et al.*, "ZnO thin-film transistor grown by rf sputtering using carbon dioxide and substrate bias modulation," *J. Nanomater.*, vol. 2014, 2014, doi: 10.1155/2014/709018.

[15] P. P. Deshpande, R. S. Pande, and R. M. Patrikar, "Fabrication and characterization of zinc oxide piezoelectric MEMS resonator," *Microsyst. Technol.*, vol. 26, no. 2, pp. 415–423, 2020, doi: 10.1007/s00542-019-04509-w.

[16] M. L. Schuette *et al.*, "Ionic Metal-Oxide TFTs for Integrated Switching Applications," *IEEE Trans. Electron Devices*, vol. 63, no. 5, pp. 1921–1927, 2016, doi: 10.1109/TED.2016.2544200.

[17] S. Gevorgian, *Ferroelectrics in Microwave Devices, Circuits and Systems*, vol. 53, no. 9. Springer-Verlag London, 2009.

[18] S. Gevorgian, A. Vorobiev, and T. Lewin, "Dc field and temperature dependent acoustic resonances in parallel-plate capacitors based on SrTiO3 and Ba0.25Sr 0.75TiO3 films: Experiment and modeling," *J. Appl. Phys.*, vol. 99, no. 12, pp. 1–11, 2006, doi: 10.1063/1.2209727.

[19] G. Rupprecht and W. H. Winter, "Electromechanical behavior of single-crystal strontium titanate," *Phys. Rev.*, vol. 155, no. 3, pp. 1019–1028, 1967, doi: 10.1103/PhysRev.155.1019.

[20] M. Z. Koohi, S. Lee, and A. Mortazawi, "Design of BST-on-si composite FBARs for switchable BAW filter application," *Eur. Microw. Week 2016 "Microwaves Everywhere", EuMW 2016 - Conf. Proceedings; 46th Eur. Microw. Conf. EuMC 2016*, pp. 1003–1006, 2016, doi: 10.1109/EuMC.2016.7824515.

[21] V. C. Lee, “Switchable and Tunable Ferroelectric Devices for Adaptive and Reconfigurable RF Circuits by,” University of Michigan, 2014.

[22] Britannica, “Tungsten,” 2019. [Online]. Available: https://www.britannica.com/science/tungsten-chemical-element. [Accessed: 10-Feb-2021].

[23] Britannica, “Platinum,” 2021. [Online]. Available: https://www.britannica.com/science/platinum. [Accessed: 10-Feb-2021].

[24] R. Ruby, “Review and comparison of bulk acoustic wave FBAR, SMR technology,” *Proc. - IEEE Ultrason. Symp.*, pp. 1029–1040, 2007, doi: 10.1109/ULTSYM.2007.262.

[25] G. Piazza, P. J. Stephanou, and A. P. Al Pisano, “Piezoelectric Aluminum Nitride Vibrating,” *J. Micromechanical Syst.*, vol. 15, no. 6, pp. 1406–1418, 2006.

[26] M. J. Hagmann, “Analysis and equivalent circuit for accurate wideband calculations of the impedance for a piezoelectric transducer having loss,” *AIP Adv.*, vol. 9, no. 8, 2019, doi: 10.1063/1.5118897.

[27] H. Chandrahalim, “Voltage Tunable Radio Frequency Microelectromechanical Resonators And Filters,” Cornell University, 2009.

[28] “QORVO IS MAKING 5G A REALITY,” 2021. [Online]. Available: https://www.qorvo.com/innovation/5g. [Accessed: 12-May-2021].

[29] G. Piazza, “Piezoelectric aluminum nitride vibrating RF MEMS for radio front-end technology,” University of California, Berkeley, 2005.

[30] Z. Chen, X. Kan, Q. Yuan, T. Wang, J. Yang, and F. Yang, “A Switchable High-Performance RF-MEMS Resonator with Flexible Frequency Generations,” *Sci. Rep.*, vol. 10, no. 1, pp. 1–15, 2020, doi: 10.1038/s41598-020-61744-2.

[31] P. J. Stephanou, G. Piazza, C. D. White, M. B. J. Wijesundara, and A. P. Pisano, “Mechanically Coupled Contour Mode Piezoelectric Ain Mems Filters,” *Sensors And Actuators*, no. January, pp. 906–909, 2006.

[32] S. Ghaffari *et al.*, “Accurate modeling of quality factor behavior of complex silicon MEMS resonators,” *J. Microelectromechanical Syst.*, vol. 24, no. 2, pp. 276–288, 2015, doi: 10.1109/JMEMS.2014.2374451.

[33] J. R. Vig and Y. Kim, “Noise in microelectromechanical system resonators,” *IEEE Trans. Ultrason. Ferroelectr. Freq. Control*, vol. 46, no. 6, pp. 1558–1565, 1999, doi: 10.1109/58.808881.

[34] Y. Wang *et al.*, “Quantification of Energy Dissipation Mechanisms in Toroidal Ring Gyroscope,” *J. Microelectromechanical Syst.*, pp. 1–10, 2021, doi: 10.1109/JMEMS.2020.3045985.

[35] R. Lifshitz and M. Roukes, “Thermoelastic damping in micro- and nanomechanical systems,” *Phys. Rev. B - Condens. Matter Mater. Phys.*, vol. 61, no. 8, pp. 5600–5609, 2000, doi: 10.1103/PhysRevB.61.5600.

[36] Y. H. Park and K. C. Park, “High-fidelity modeling of MEMS resonators - Part I: Anchor loss mechanisms through substrate,” *J. Microelectromechanical Syst.*, vol. 13, no. 2, pp. 238–247, 2004, doi: 10.1109/JMEMS.2004.825300.

[37] S. A. Chandorkar, M. Agarwal, R. Melamud, R. N. Candler, K. E. Goodson, and T. W. Kenny, “Limits of quality factor in bulk-mode micromechanical resonators,” *Proc. IEEE Int. Conf. Micro Electro Mech. Syst.*, pp. 74–77, 2008, doi: 10.1109/MEMSYS.2008.4443596.

[38] J. Baborowski, C. Bourgeois, A. Pezous, C. Muller, and M. A. Dubois, “Piezoelectrically activated silicon resonators,” *Proc. IEEE Int. Freq. Control Symp. Expo.*, pp. 1210–1213, 2007, doi: 10.1109/FREQ.2007.4319269.

[39] K. M. Lakin, “Thin film resonator technology,” *IEEE Trans. Ultrason. Ferroelectr. Freq. Control*, vol. 52, no. 5, pp. 707–716, 2005, doi: 10.1109/TUFFC.2005.1503959.

[40] Y. Wang *et al.*, “Well-controlled wet etching of ZnO films using hydrogen peroxide solution,” *Appl. Surf. Sci.*, vol. 292, pp. 34–38, 2014, doi: 10.1016/j.apsusc.2013.11.053.

[41] D. G. Yoo *et al.*, “Fabrication of the ZnO thin films using wet-chemical etching processes on application for organic light emitting diode (OLED) devices,” *Surf. Coatings Technol.*, vol. 202, no. 22–23, pp. 5476–5479, 2008, doi: 10.1016/j.surfcoat.2008.06.064.

[42] T. Zhang, L. Sun, D. Han, Y. Wang, and R. Han, “Surface uniform wet etching of ZnO films and influence of oxygen annealing on etching properties,” *NEMS 2011 - 6th IEEE Int. Conf. Nano/Micro Eng. Mol. Syst.*, pp. 626–629, 2011, doi: 10.1109/NEMS.2011.6017433.

[43] M. C. Peignon, C. Cardinaud, and G. Turban, “Etching processes of tungsten in SF6-O2 radio-frequency plasmas,” *J. Appl. Phys.*, vol. 70, no. 6, pp. 3314–3323, 1991, doi: 10.1063/1.350347.

[44] J. Bühler, F. P. Steiner, and H. Baltes, “Silicon dioxide sacrificial layer etching in surface micromachining,” *J. Micromechanics Microengineering*, vol. 7, no. 1, 1997, doi: 10.1088/0960-1317/7/1/001.

[45] P. A. Köllensperger, W. J. Karl, M. M. Ahmad, W. T. Pike, and M. Green, “Patterning of platinum (Pt) thin films by chemical wet etching in Aqua Regia,” *J. Micromechanics Microengineering*, vol. 22, no. 6, p. 067001, 2012, doi: 10.1088/0960-1317/22/6/067001.

[46] Adam Olzick, “DEPOSITION, CHARACTERIZATION, AND FABRICATION OF A ZINC OXIDE PIEZOELECTRIC THIN FILM MICROSPEAKER USING DC REACTIVE SPUTTERING,” California Polytechnic State University, 2012.

[47] M. Wei, A. Avila, I. Rivera, M. Baghelani, and J. Wang, “ZnO on nickel RF micromechanical resonators for monolithic wireless communication applications,” *J. Micromechanics Microengineering*, vol. 27, no. 5, 2017, doi: 10.1088/1361-6439/aa635c.

[48] A. Gao, K. Liu, J. Liang, and T. Wu, “AlN MEMS filters with extremely high bandwidth widening capability,” *Microsystems Nanoeng.*, vol. 6, no. 1, 2020, doi: 10.1038/s41378-020-00183-5.

[49] R. Serhane *et al.*, “PLD elaboration of piezoelectric ZnO thin film for 540 MHz Al/ZnO/Pt bulk acoustic wave resonator,” *2013 Jt. IEEE Int. Symp. Appl. Ferroelectr. Work. Piezoresponse Force Microsc. ISAF/PFM 2013*, pp. 275–278, 2013, doi: 10.1109/ISAF.2013.6748667.

REPORT DOCUMENTATION PAGE	Form Approved OMB No. 0704-0188

1. REPORT DATE *(DD-MM-YYYY)*	2. REPORT TYPE	3. DATES COVERED *(From - To)*
17-06-2021	Master's Thesis	September 2019-June 2021

4. TITLE AND SUBTITLE

Feasibility Study of Radio Frequency Microelectromechanical Filters for Space Applications

5a. CONTRACT NUMBER

5b. GRANT NUMBER

5c. PROGRAM ELEMENT NUMBER

6. AUTHOR(S)

Singh, Karanvir, 1st Lt

5d. PROJECT NUMBER

5e. TASK NUMBER

5f. WORK UNIT NUMBER

7. PERFORMING ORGANIZATION NAME(S) AND ADDRESS(ES)

Air Force Institute of Technology
Graduate School of Engineering and Management (AFIT/ENG)
2950 Hobson Way
Wright-Patterson AFB OH 45433-7765

8. PERFORMING ORGANIZATION REPORT NUMBER

AFIT-ENG-MS-21-J-016

9. SPONSORING/MONITORING AGENCY NAME(S) AND ADDRESS(ES)

Air Force Research Labs Space Vehicles
Dr. Madeleine Naudeau, PI of Advanced GPS Technologies
2000 Wyoming Blvd SE
Albuquerque, NM 87123
madeleine.naudeau@us.af.mil

10. SPONSOR/MONITOR'S ACRONYM(S)

AFRL/RV

11. SPONSOR/MONITOR'S REPORT NUMBER(S)

12. DISTRIBUTION/AVAILABILITY STATEMENT

DISTRUBTION STATEMENT A. APPROVED FOR PUBLIC RELEASE; DISTRIBUTION UNLIMITED.

13. SUPPLEMENTARY NOTES

14. ABSTRACT

Piezoelectric contour mode resonator technology has the unique advantage of combining low motional resistance with the ability to define multiple frequencies on the same substrate. Contour mode resonators can be mechanically coupled together to form robust band-pass filters for the next generation of GPS satellites with extreme size reduction compared to electrically coupled filters. Piezoelectric zinc oxide (ZnO) contour mode resonators have the potential for monolithic integration with current ZnO transistor further reducing size, power consumption, and cost of filter modules. Barium strontium titanate (BST) contour mode resonators have incredible frequency tunability due to the fundamental nature of the thin film in the presence of a DC bias. BST resonators can be intrinsically switched on and off with the application of a DC bias. Through this research, the feasibility of the design and fabrication of piezoelectric radio frequency (RF) microelectromechanical system (MEMS) filters using ZnO, BST, and metals with high melting points is presented.

15. SUBJECT TERMS

16. SECURITY CLASSIFICATION OF:			17. LIMITATION OF ABSTRACT	18. NUMBER OF PAGES	19a. NAME OF RESPONSIBLE PERSON
a. REPORT	b. ABSTRACT	c. THIS PAGE			Dr. Hengky Chandrahalim, AFIT/ENG
U	U	U	UU	96	19b. TELEPHONE NUMBER *(Include area code)* (937) 255-6565 x4483 Hengky.Chandrahalim@afit.edu